Maryami, R., Showkat Ali, S. A., Azarpeyvand, M., & Afshari, A. (2020). Turbulent flow interaction with a circular cylinder. *Physics of Fluids*, *32*(1), [015105 (2020)]. https://doi.org/10.1063/1.5119967

Peer reviewed version

Link to published version (if available):
10.1063/1.5119967

Link to publication record in Explore Bristol Research
PDF-document

This is the author accepted manuscript (AAM). The final published version (version of record) is available online via AIP Publishing at https://aip.scitation.org/doi/10.1063/1.5119967. Please refer to any applicable terms of use of the publisher.

University of Bristol - Explore Bristol Research

General rights

This document is made available in accordance with publisher policies. Please cite only the published version using the reference above. Full terms of use are available:
http://www.bristol.ac.uk/pure/about/ebr-terms

Turbulent flow interaction with a circular cylinder

Reza Maryami,[1, a)] Syamir Alihan Showkat Ali,[2] Mahdi Azarpeyvand,[3, b)] and Abbas Afshari[1]

[1)] *Yazd University, Yazd, Iran.*

[2)] *School of Manufacturing, University Malaysia Perlis, Malaysia.*

[3)] *University of Bristol, Bristol, UK.*

(Dated: 30 November 2019)

This paper presents a comprehensive experimental study on the unsteady pressure exerted on the surface of a round cylinder in smooth and turbulent flows. A highly instrumented cylinder with several static pressure taps and dynamic pressure transducers at different spanwise and peripheral locations was used, enabling extensive dynamic surface pressure, coherence and turbulence length-scale analysis. The effects of the free-stream turbulence and turbulent length scale are investigated by placing the turbulent-generating grids within the wind tunnel duct. For both the laminar and turbulent incident flows, the surface pressure results show the emergence of the fundamental, first and second harmonics at most peripheral angles, while at the cylinder base the surface pressure spectra is dominated by the first harmonic. It has also been observed that an increase in the level of the turbulence intensity results in the increase of the energy level of unsteady pressure acting on the cylinder. An increase in the length scale of the incoming flow structures is shown to result in an increase in the energy level of the tonal frequencies and the broadband content of the surface pressure spectra. The spanwise coherence results have also shown that an increase in the length scale of the flow structures increases the spanwise correlation length of the flow structures at the vortex shedding frequency at the stagnation point, while at the cylinder base, the spanwise correlation length decreases at the vortex shedding frequency.

[a)] Electronic mail: r.maryami@gmail.com

[b)] Electronic mail: m.azarpeyvand@bristol.ac.uk

I. INTRODUCTION

The aerodynamics of circular cylinders placed in a laminar[1] and turbulent cross-flow[2] (*i.e.* perpendicular to the longitudinal axis) has been extensively studied as it contains some very interesting physics and is of great importance in many engineering applications, including bridges, chimneys, tubular heat exchangers, risers in marine engineering and so on. The flow over bluff bodies and the methods to reduce the associated noise and vibration are also of great academic and industrial interest[3–12]. While the aerodynamics of bluff bodies has been the subject of much experimental studies, there still exists a need for high-quality measurement to better understand the effects of free-stream turbulence on the aerodynamic performance of the cylinder, including the unsteady forces acting on the cylinder.

The flow induced tones, *i.e.* Aeolian tone, generated due to the periodic vortex shedding within the wake region of the cylinder known as a basic and important characteristic of the aerodynamic of bluff bodies and the emergence of such tones has also been observed in other experimental studies[8,13,14]. The effects of free-stream turbulence flow and the turbulence length scale on the vortex shedding from the cylinder have been investigated in the literature but many features are still unclarified. The effects of turbulent incident flow on the dynamic flow around bluff bodies, particularly at high Reynolds number have been clearly reviewed by Bearman and Morel[15]. It is well know that the Reynolds sub-critical regime (*i.e.* $Re = 300 - 2\times10^5$) is characterized by laminar separation and the formation of the turbulent vortices in the downstream region. Transition was reported to move upstream with the increase in turbulence intensity and/or Reynolds number[16], leading to increase mixing which indicates that the vortex formation occurs closer to the cylinder base[17]. The shrinking of the vortex formation region can also be attributed with the decrease in the base pressure and increase in the fluctuating forces. Norberg and Sunden[18] provides some important results based on the experimental study on the effects of the Reynolds number and turbulence intensity on the fluid flow acting on a circular cylinder. An increase in the pressure forces with increasing turbulence intensity is observed for $Re < 10^5$, while that an opposite trend are noticed for higher Reynolds number. West and Apelt[6] have carried out experiments on the fluctuating pressure distributions, *i.e.* root-mean-square (rms) forces, in sub-critical flow on laminar circular cylinder. Results show that the effects of changes in the free-stream turbulence on the mean drag coefficient, rms lift coefficient and rms pressure distributions are similar to that of the influences

of the increase in the Reynolds number.

The directivity of the noise radiated by circular cylinders was first investigated by Stowell and Deming[8] and showed that the noise field peaks normal to the free-stream of the flow direction and the cylinder axis and has a dipolar character. Curle[19] showed theoretically that that the fluctuating forces acting on the cylinder leads to a dipolar radiation. It can be inferred that the unsteady pressure exerted on the body of the cylinder is directly related to the far-field sound from a circular cylinder due to the interaction with the boundary layer and wake flow turbulence structures[11]. In order to better understand the noise generation mechanism from the external bodies in a fluid flow, it is imperative to study the flow-field around the cylinder and the associated unsteady forces exerted by the flow structures. The unsteady surface pressure fluctuations acting on the surface in a flow field can be measured via a conventional method using the miniature pressure transducers. Schlinker *et al.*[4] have performed an extensive study on a vortex shedding noise from a circular cylinder using the miniature pressure transducers. The results had demonstrated that the vortex shedding is dependent on the effective Reynolds number and the surface roughness. In order to understand the statistical characteristics of the wake flow structures, Casalino and Jacob[20] have also carried out the surface pressure fluctuation measurements using the miniature pressure transducers. The results indicate that the lift fluctuation force acting on the cylinder is related to the fundamental vortex shedding frequency and the second harmonic, while the drag fluctuations of the cylinder correspond to the first harmonic frequency. The investigation of the vortex shedding tone and the wall pressure fluctuations using the same measurement methods has also been carried out by Oguma *et al.*[11], Fujita *et al.*[21] and Ackerman *et al.*[22] over a wide range of Reynolds numbers.

As reviewed above, most of the works carried out to date have been experimental, with the majority of it in wind tunnels with low levels of free-stream turbulence. There is, therefore, a need for better understanding of the steady and unsteady aerodynamic response of bluff bodies in turbulent flows. Also, the surface pressure fluctuations over the circumference of the cylinder and along its span in turbulent incident flow have rather received little attention. This study aims to provide an extensive body of research on the unsteady pressure exerted on the surface of circular cylinders in a turbulent cross-flow in the subcritical flow[23] (*i.e.* transition to turbulence in the free shear layer) regime. In what follows, a comprehensive aerodynamic and near-field correlation studies have been carried out on the surface of a round cylinder in laminar and turbulent flows to

improve our understanding on the turbulent flow interaction with bluff bodies. The experimental setup and wind tunnel tests are described in Sec. II. The grid turbulence characterization will be discussed in Sec. III. The results and discussions are detailed in Sec. IV. Finally, Sec. V concludes and summarizes our findings on the effect of a turbulent flow interaction with a circular cylinder.

II. MEASUREMENT SETUP

The flow experiments were performed in an open-jet subsonic wind tunnel facility with an exit cross-sectional area of 0.46 $m \times 0.46$ m. The wind tunnel can reach a maximum reliable wind speed of 25 m/s and a turbulence level of less than 0.3% without the turbulence generating grids. In order to study the turbulence interaction effects, a grid is installed upstream of the duct exit for generating turbulence. A rectangular long duct is placed after the contraction nozzle in order to enable the proper placement of the grids at different locations, as shown in Fig. 1. The performance of the duct and the flow quality will be further discussed in the following section. The internal walls of the wind tunnel were treated with a highly absorbing porous layer[24] to reduce any noise contamination due to the fan background noise. The use of the walls with absorbing porous layer was found to reduce the fan background noise by 15 dB over the frequency range of interest.

A. Cylinder configuration

The flow measurements have been carried out using a circular cylinder with an outer diameter of $D = 22$ mm and a span length of $L = 460$ mm. The circular cylinder test-rig is made of three different parts, consisting of one middle section with static and dynamic surface pressure instrumentations and two side extension parts. The layout of the circular cylinder setup is shown in Fig. 1. In order to minimize the wind tunnel wall effects on the measured quantities, the model was built with an aspect ratio (L/D) of over 20 (Ref.[25]). The blockage ratio of the cylinder was found to be less than 5%. The cylinder was properly placed within the potential core of the nozzle jet flow and was held by two parallel rectangular side-plates to ensure two-dimensional flow over the cylinder and avoid vibration. The test-rig was mounted on a turning-table to collect pressure data in fine angular increments, *i.e.* at every 5° degrees. In what follows, the ($x^{'}$, $y^{'}$, $z^{'}$) coordinate system, placed on the turbulence grid, will be used to define the flow quantities related to the grid.

The (X, Y, Z) coordinate system, placed at the duct exit, will be used for defining the location of the cylinder. Finally, the (x, y, z) coordinate system, located at the center and mid-span of the cylinder, will be used for all other results presented in the paper. A general schematic of the nozzle, turbulence grid, and the coordinate systems are provided in Fig. 1.

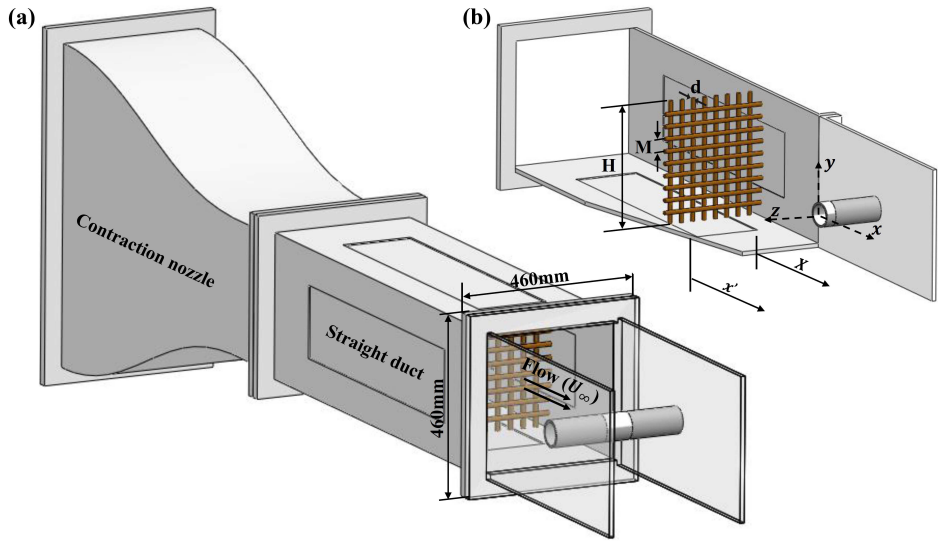

FIG. 1: (a) The geometry of the contraction nozzle and the experimental setup, (b) turbulence-generating grid placed at X/M=-20 upstream of the duct exit.

B. Static pressure measurement

In order to better understand the flow field around the cylinder, the test-rig was instrumented with 18 static pressure taps, which are distributed evenly over the circumference of the cylinder with an angular spacing of 20°, see Fig. 2. The static pressure taps have a diameter of 0.55 mm. The pressure taps were tightly fitted with a 5 mm long brass tube, with the inner and outer diameters of 0.4 mm and 0.6 mm, respectively. The brass tubes are connected to flexible polyurethane tubes, and finally connected to the pressure scanner ports. A 16 channels Honeywell electronic differential pressure measurement was used to perform the static pressure measurements. The scanners have a full-scale measuring capacity of ranges up to ±2.48 kPa with a system accuracy of ±2%. An uncertainty analysis was carried out, based on the method described in Ref.[26], and the uncertainty was found to be below 2.2%.

C. Surface pressure instrumentation

The cylinder was instrumented with several Panasonic electret condenser pressure transducer (series WM-61A) for the measurement of the unsteady surface pressure fluctuations. The transducers have a diameter of 6 mm, height of 3.4 mm and circular sensing area of 2 mm. The same type of pressure transducer was previously used in other studies[27], which has shown to produce reliable pressure data over the frequency range of interest (100Hz $\leq f \leq$ 10 kHz). In order to eliminate the pressure averaging effects at high frequencies, the pressure measurements were carried out using a small pinhole with a very small diameter at the surface of the cylinder[3,10,28,29]. The pressure transducers are placed underneath a small pinhole mask of 0.55 mm diameter and fixed inside the cylinder using a fully sealed holding mechanism, see Fig. 2. A total number of 15 pressure transducers are distributed in the spanwise and peripheral directions of the cylinder. The layout of the pressure transducers is shown in Fig. 2. In order to verify the two-dimensionality of the flow and to measure the spanwise length scale of the flow structure, a set of transducers (*p1-p8*) are installed along the span of the cylinder. The transducers in the spanwise direction are placed with an unequal spacing, which provides a non-redundant population of sensor spacing and a maximum number of spatial distances for correlation studies[5]. The spanwise transducers are distributed over $6D$ to enable the proper capture of large two-dimensional flow structures[21,27,30].

It is important to ensure that the transducers are kept outside of the boundary layer developed over the surface of the side-plates. In this study, the wall boundary layer thickness was measured using a single-hotwire probe at both sides of the side-plates. The maximum wall boundary layer thickness formed as a result of the side-plates at the flow velocity of $U_\infty = 10\ m/s$ was found to be nearly 4 mm. In order to better understand the flow structures and flow shedding around the cylinder, several pressure transducers (*p9-p15*) are distributed over the circumference of the cylinder at the mid-span plane with an angular spacing of 45°. The locations of the in-situ pressure transducers are summarized in Table I. The transducers were calibrated in-situ based on the method described in Ref.[1], and the calibration was performed before and after each measurement. A 16-channel NI PCI-6023E data acquisition system was used to collect the surface pressure fluctuations data, with a sampling frequency of 40 kHz and time duration of 60 seconds. In order to reduce the statistical convergence error, the pressure spectra were calculated based on the average spectra of individual data obtained from dividing the time series pressure data into a sequence of

blocks[31], *i.e.* $1/\sqrt{N_r}$, N_r is the number of records. In the present work, a total number of N_r=384 records were used, leading to an uncertainty level of about 5.1%.

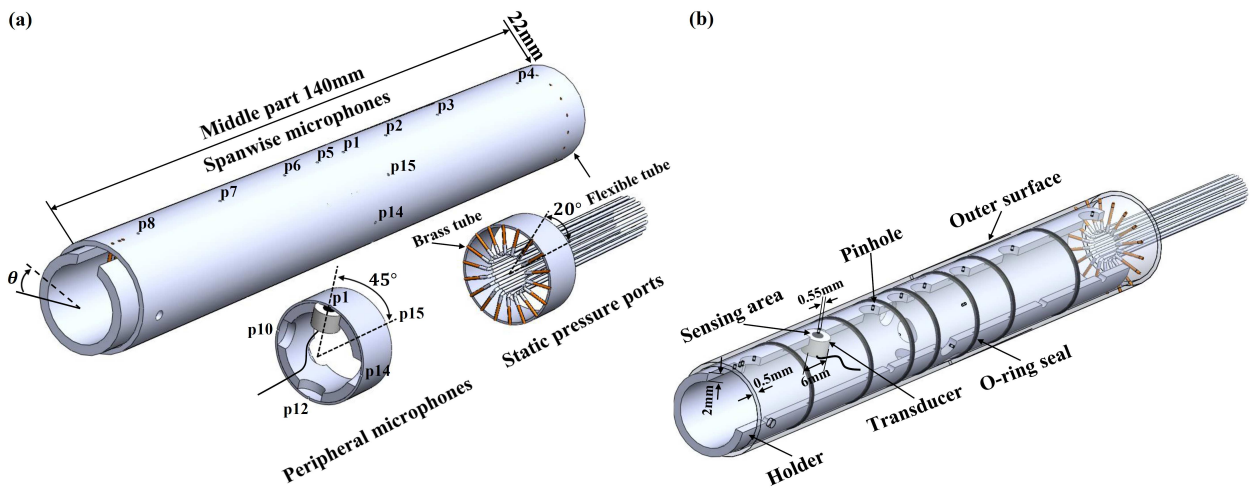

FIG. 2: (a) In-situ boundary layer surface pressure measurement using a pressure transducer installed under a pinhole and (b) The sensing area on the cylinder equipped with static pressure taps and spanwise and peripheral pressure transducers.

TABLE I: Position of pressure pinholes on the surface of model.

Transducers	z/D	θ	**Transducers**	z/D	θ
p1	0.0	90°	*p9*	0.282	45°
p2	0.682	90°	*p10*	0.0	0°
p3	1.545	90°	*p11*	0.282	−45°
p4	2.955	90°	*p12*	0.0	−90°
p5	-0.41	90°	*p13*	0.282	−135°
p6	-0.91	90°	*p14*	0.0	180°
p7	-1.864	90°	*p15*	0.282	135°
p8	-3.0	90°	-	-	-

D. Hot-wire anemometry set-up

The flow mean velocity and turbulence level were measured using a single hot-wire probe with a standard tungsten wire of 5 μm diameter and length of 1.25 mm. The hot-wire probe was calibrated both statically and dynamically by a standard Pitot tube and the signals were low-pass filtered by a cut-off frequency of 30 kHz before they were A/D converted. The calibration process was performed before and after each measurement. The data have been recorded using a 16-channel NI PCI-6023E data acquisition system with a sampling frequency of 25 kHz and for a sampling time of 20 seconds at each location. The probe was traversed in the flow using a three-axis traverse unit controlled by stepper motors with a typical minimum positioning accuracy of 0.01 mm. The uncertainty of the measured velocity signals, obtained using the methodology described in Ref.[26], was found to be below 3.8%.

III. GRID TURBULENCE CHARACTERIZATION

In order to produce a turbulent flow, with desirable turbulence level and length scale, three biplane grids with different mesh sizes were used in the present work. The shape of the grid elements can have important effects on the homogeneity, turbulence intensity level and the stability of the wake flow-field generated by the grid elements[32]. In order to ensure the production of an approximately homogeneous turbulent region, Corrsin[32] suggested that the grid must be designed such that $H >> M$, where H is the wind tunnel cross-section dimension and M is the mesh length of the grid.

The biplane grids are usually built using either square bars or round rods. In the present study, the biplane grids are made of round rods due to its capability in generating relatively larger and more periodic turbulent flow structures downstream of the grid compared to that of the square bars[33]. The diameter of the round rods used here is determined based on the mesh size ratio, $M/d \approx 5$, as suggested Laws and Livesey[34].

Another important geometrical parameter for a turbulence grid is the grid solidity, defined as the projected solid area per unit total area[35], $\sigma = (d/M) \times (2 - d/M)$. Laws and Livesey[34] stated that the grids with a solidity value range of σ=35%-40% can generate homogeneous and isotropic turbulence at sufficiently large distances downstream of the grid. The grids with large solidity

ratios, *i.e.* above 50%, tend to generate less homogeneous, isotropic turbulence, and should be avoided[36]. Based on the criteria defined above, three different grids were designed, manufactured and tested as part of this study. The geometric parameters of the three grids used in this study are tabulated in Table II.

1. Grid flow field regions

The flow field downstream of a turbulence grid can be divided into three main regions. The first region corresponds to the flow developing region immediately after the grid. The flow in this region is inhomogeneous and anisotropic, and consequently, the production of turbulent kinetic energy is observed[37]. The second region is dominated by a flow which is nearly homogeneous and isotropic. Depending on the Reynolds number of the flow, the second region is found to begin at a distance of $10M$ to $50M$ downstream of the grid[38,39]. This region is found to be the appropriate location for the positioning of the circular cylinder for turbulence interaction studies. The final region lies far downstream of the grid where a rapid decay of turbulence is observed. Corrsin[32] suggested that for grids with a relatively low solidity, the flow measurements should be performed at $x^{'}/M \geq 40$. However, several empirical studies[40–42] have shown that the second region may exist as early as $x^{'}/M \approx 20$. In the present study, the flow measurement locations of all the three biplane grids were chosen along the center line of the tunnel, within the spatial range of $20 \leq x^{'}/M \leq 80$. The turbulence-generating grid for all the three cases is always installed at X/M=-20 (*i.e.* $x^{'}$=800 mm, 1128 mm and 1800 mm for grids 1, 2 and 3, respectively), upstream of the duct exit, as shown in Fig. 1.

2. Turbulence intensity level and length scales

The turbulence intensity level can be calculated from the measured mean square velocity, as $Tu = \sqrt{\overline{u'^2}}/U_\infty$. The turbulence length scale, on the other hand, can be estimated from two different methods, namely (a) Von Karman spectrum data fitting and (b) integration of the auto-correlation curve. The results from these two methods will be compared against each other later. The Von Karman spectrum for an isotropic turbulence[43] can be found from,

$$\frac{\phi_{uu}^{VK}(f)U_\infty}{\overline{u'^2}\Lambda_{uu}} = 4\left(1+\left(\frac{8\pi f\Lambda_{uu}}{3U_\infty}\right)^2\right)^{-5/6}, \tag{1}$$

where $\phi_{uu}^{VK}(f)$ is the Von Karman spectrum. Since the hotwire data can provide the velocity energy spectrum (ϕ_{uu}), mean velocity (U_∞) and also the mean squared velocity ($\overline{u'^2}$), the value of the turbulence length scale (Λ_{uu}) can be easily found by curve fitting.

Alternatively, the integral scale of the turbulence structures (Λ_{uu}) can also be determined using the velocity autocorrelation of the velocity fluctuations[36]. The velocity autocorrelation can be found from,

$$R_{uu}(\tau) = \frac{\overline{u'(t)u'(t+\tau)}}{\overline{u'^2}}, \tag{2}$$

where the u' is the velocity fluctuation, τ is the time delay and overbar represents the time-averaging. The integral length scale of the flow structures (Λ_{uu}) can then be calculated using the velocity autocorrelation data as,

$$\Lambda_{uu} = U_\infty \int_0^\infty R_{uu}(\tau)\, d\tau. \tag{3}$$

In order to determine the location of the cylinder for all the three biplane grids, the velocity fluctuation data have been collected at 36 positions ($0 \leq X/D \leq 16.36$) downstream of the nozzle. The locations of the cylinder for each grid have been chosen based on the changes in the turbulence intensity level and the turbulence length scale obtained along the centerline of the nozzle, as shown in Fig. 3. The dashed square line in Fig. 3 represents the locations of the cylinder, which are also tabulated in Table II. The turbulence intensity level and the turbulence length scale at the selected locations are also provided in Table II.

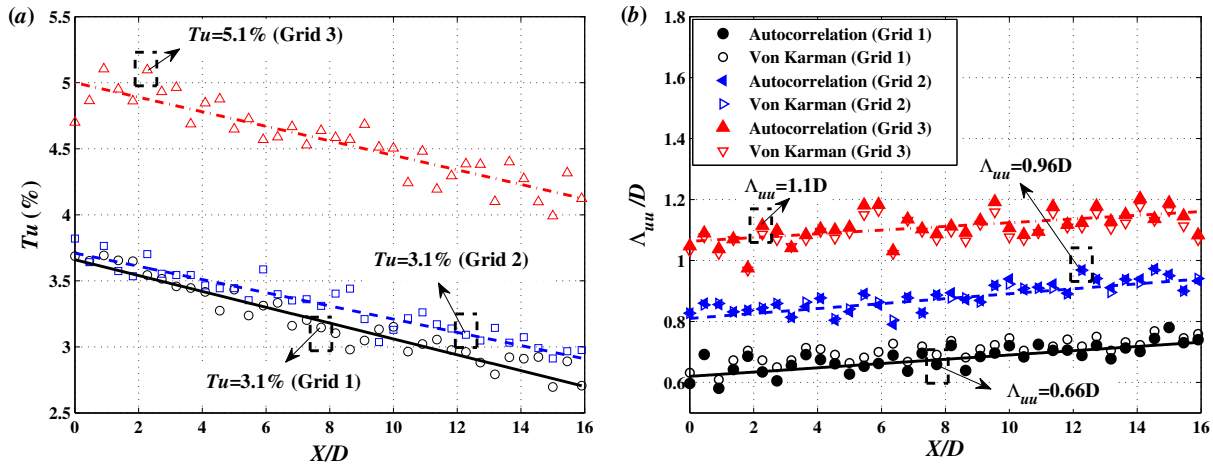

FIG. 3: (a) Variations of turbulence intensity along centerline in the wake downstream of three biplane grids at $Re = 14.7 \times 10^3$ and (b) Comparison of calculated turbulence length scale using auto correlation and Von Karman spectrum methods. The squares with dashed line and the arrows indicate the selected location of the cylinder. Note that the turbulence measurements were always performed at 20 mesh lengths downstream from the grid ($20 \leq x^{'}/M \leq 80$)

TABLE II: The positions of the cylinder, variation of the turbulence intensity level, the turbulence length scale downstream of the biplane grids 1, 2 and 3 and the geometrical properties of turbulence grid used in this study.

Grids	**Cylinder position**		Tu	Λ_{uu}/D	d (mm)	M (mm)	M/d	σ
	X/D	$x^{'}/M$						
Grid 1	2.72	24.25	3.1%	0.66	9	40	4.44	40%
Grid 2	12.27	24.78	3.1%	0.96	12.7	56.4	4.44	40%
Grid 3	2.27	20.55	5.1%	1.1	20.3	90	4.43	40%

The choice of these locations will give us the opportunity to compare the effect of the changes in the turbulence intensity for a fixed length scale (*i.e.* grids 2 and 3) or the effect of the changes in the flow length scale at a fixed turbulence intensity (*i.e.* grids 1 and 2). The results in Fig. 3(a)

generally show that the turbulence intensity level decreases along the centerline of the wake. The turbulence length scale, on the other hand, increases as the turbulent eddies move downstream from the grid due to the inertial effects of the turbulent eddy, see Fig. 3(b).

In order to analyze the properties of the flow at the proposed locations listed in Table II, a comparison between the power spectral density of the velocity fluctuations and the Von Karman spectrum for all three grids is provided in Fig. 4. The results show that the velocity power spectral density for all three biplane grids at selected measurement locations fit well with the theoretical Von Karman spectrum. As expected, in the case of an isotropic turbulence flow, the velocity spectrum follows a slope of -5/3.

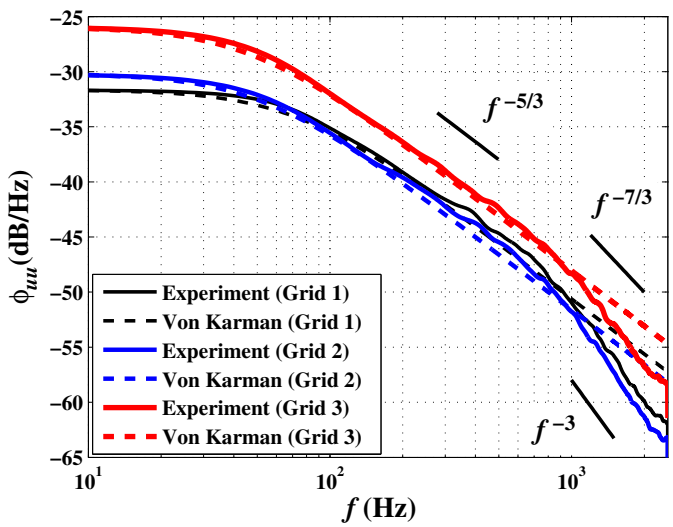

FIG. 4: Comparison of the measured streamwise velocity spectrum against Von Karman curve-fit at $Re = 14.7 \times 10^3$. The measurement locations are provided in Table II.

IV. RESULTS AND DISCUSSIONS

A. Aerodynamic characteristics

The results of the static pressure distribution around the cylinder are presented in this subsection, which also serve as a validation of the experimental setup and the wind tunnel used in the present work. The experiments were performed with and without the turbulence generating grids (grids 1, 2 and 3) at the free-stream velocity of U_∞=10 m/s, corresponding to the Reynolds number

of Re=14.7 $\times$ 10^3, *i.e.* within the subcritical regime. Figure 6(a) compares the variation of the mean pressure coefficient data measured for all the three biplane grids (turbulent incident flow) against the data measured without the grid (laminar incident flow). Some other experimental data available in the literature at different turbulence intensity levels[17,44] are also provided for comparison and validation purposes. The pressure coefficient results ($C_p = (p - p_\infty)/(0.5\rho U_\infty^2)$) are presented only for the top side of the cylinder, *i.e.* $\theta = [0^o - 180^o]$. In what follows, the square brackets, [θ_1,θ_2], denotes the angular range between the angular locations θ_1 and θ_2 over the cylinder. The pressure coefficient minimum point and starting-point of the base region are denoted by θ_m and θ_s for the laminar incident flow and θ_m^G and θ_s^G for the turbulent incident flow, respectively. The base point, *i.e.* $\theta = 180^o$ is denoted by θ_b for both flow cases. A sketch of a typical flow pattern formed around a cylinder is provided in Fig. 5. At the front of the cylinder ($\theta = 0^o$), a stagnation point is formed where the oncoming flow is brought to rest. The separation point at θ_s defined as the point where the vorticity is equal to zero at the surface. The cylinder base ($\theta = 180^o$) is also shown in Fig. 5. The pre- and post-separation region, wake region,flow streamline and the boundary layer edge of the flow are also defined in Fig. 5.

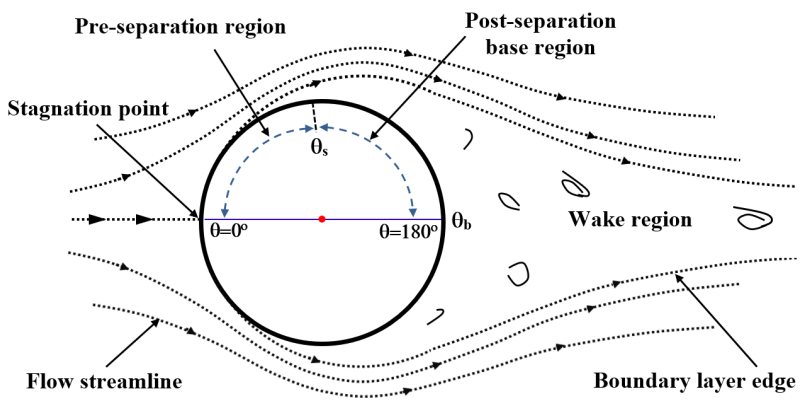

FIG. 5: A schematic of flow interaction with a cylinder. The schematic shows the location of the stagnation point, separation point (θ_s), pre- and post-separation regions and the cylinder base (θ_b).

In the favourable pressure gradient region, *i.e.* from the stagnation point to the point of minimum pressure (θ_m and θ_m^G), as expected, all curves give a value of $C_p \approx$1 at the stagnation point ($\theta = 0°$), followed by a rapid decay and becoming negative at around $\theta = 35^o$. The minimum

pressure coefficient for the laminar incident flow is observed to occur at the angular position $\theta_m = 70^o$. In contrast, the minimum pressure coefficient for the turbulent incident flow shifts to an angular position of $\theta_m^G = 75^o$ for all the turbulent flow cases. Results have also shown that the magnitude of the minimum C_p in turbulent flow cases is smaller (more negative) than that of the laminar flow case.

In the adverse pressure gradient region, *i.e.* from the point of minimum pressure up to the starting point of the base region (θ_s and θ_s^G), the C_p becomes much smaller in the case of the turbulent incident flow, with a longer angular extent θ_{sm}^G in the adverse pressure gradient region compared to that of the laminar incident flow condition. The results in Fig. 6(a) show that the angular extent in the case of the laminar incident flow is about $\Delta\theta_{sm} = [\theta_s - \theta_m] = 10^o$ and reaches about $\Delta\theta_{sm}^G = [\theta_s^G - \theta_m^G] = 15^o$ in the case of the turbulent incident flow, similar to the results in Ref.[45].

In the base region, *i.e.* from the starting point of the base region (θ_s and θ_s^G) to the base point (θ_b), a shorter base region is observed as a result of the widening of the adverse pressure gradient region for the turbulent cases than that of the laminar flow case. The difference between the base regions in both the laminar and turbulent incident flows include a higher negative pressure coefficient in the case of the turbulent incident flow, see Fig. 6(a). The decrease in the base pressure is due to the increasing curvature of the free streamline and entrainment of the reversed flow into the opposing shear layer, which corresponds to the reduction of the vortex formation length and enhancement of the diffusion length[17].

Figure 6(b) shows the comparison of the root-mean-square (rms) pressure coefficient data measured for all the laminar and three turbulent flow cases. The rms pressure coefficient ($C_{p_{rms}}$) results are presented only for the top side of the cylinder model $\theta = [0^o - 180^o]$. In general, the $C_{p_{rms}}$ results show that the turbulent incident flow produces a higher $C_{p_{rms}}$ acting on the cylinder compared to the laminar incident flow at all the angles. The $C_{p_{rms}}$ for the case of laminar and turbulent incident flow gradually increases and reaches a maximum value at the starting point of the base region (θ_s and θ_s^G), which occurs at an angular position of $\theta = 80^o$ for the laminar flow and $\theta = 90^o$ in the case of turbulent incident flow. This is a typical case of sub-critical flow, where the laminar boundary layer separates from the cylinder in the vicinity of separation point (θ_s). The separation region shown in Figs. 5 and Fig. 6(b)), is influenced by the periodic formation of vortex shedding into the wake and is Reynolds number dependent[6]. The emergence of a maximum

$C_{p_{rms}}$ in the vicinity of separation point is consistent with the findings by Achenbach[46] and West and Apelt[6]. The $C_{p_{rms}}$ then gradually reduces beyond θ_s and θ_s^G and reaches a minimum value at the angular position of $\theta = 120^o$. In the base region, it can be observed that both the laminar and turbulent flows exhibit an overall increase in $C_{p_{rms}}$ between $\theta = 140^o$ to $\theta = 180^o$, although the rate of $C_{p_{rms}}$ increase is much higher in the case of the turbulent flow. The $C_{p_{rms}}$ results have shown the emergence of a local peak at $\theta = 160^o$ in the case of the laminar incident flow, and at $\theta = 170^o$ with a higher amplitude in the case of the turbulent incident flows. The second maximum of $C_{p_{rms}}$ at $\theta = 160^o$ is associated with the strength of the vortices shed and shrinking of the vortex formation region[6]. In other words, the increase in the fluctuations in the base region is due to the development of a stronger vortices at the vicinity of the cylinder surface.

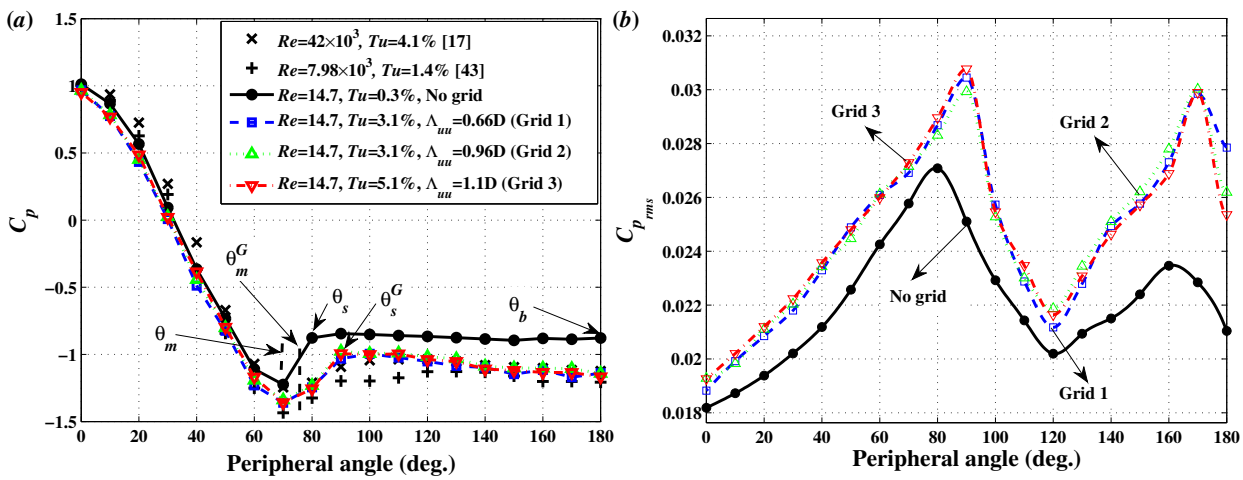

FIG. 6: (a) Mean and (b) rms pressure coefficient distributions in turbulent and laminar incident flows at $Re = 14.7 \times 10^3$.

The increase of the peak at $\theta = 170^o$ for the turbulent inflow case compared to that of the laminar flow might be due to the difference in the pressure coefficient between the two flows as illustrated in Fig. 6(a). The results show that the turbulent incident flow exhibits a higher negative pressure compared to the laminar flow. Note that, the decrease in the base pressure is due to the increasing curvature of the free streamline and entrainment of reversed flow into the opposing shear layer which corresponds to reduction of the vortex formation length and enhancement of the diffusion length[17]. The strength of the vortex increases with decreasing frequency. The results in

Figs. 8 and 9 clearly show that the in the case of the turbulent incident flow, the fundamental tonal frequency is slightly shifted to the lower frequencies compared to the laminar incident flow, which is consistent with the results of Hutcheson and Brooks[30]. Hence, it can be inferred that the vortices shed from the cylinder for the turbulent inflow case possess higher strength compared to that of the laminar flow, which leads to the increase in the $C_{p_{rms}}$ results $\theta = 170^o$ for the turbulent inflow case. Despite the overall increase in the unsteady surface pressure over the cylinder in the case of turbulent incoming flow, the largest increase is observed in the base region of the cylinder. This will be further studied in Sec. IV E.

B. Cylinder wake velocity profile

Figure 7 shows the mean and rms velocity profiles in the wake of the cylinder for the laminar and turbulent flow cases. The measurements have been carried out using a single hotwire and the data have been collected over a large domain of $0 \leq y/D \leq 4$ and $0 \leq x/D \leq 6$.

The mean velocity results at $x/D = 0.5$ (Fig. 7a) clearly show that the profile for the laminar incident flow is almost flat, *i.e.* having an almost constant velocity between $y/D = 0$ and $y/D = 0.5$, which is consistent with the results observed in previous studies[12]. The results for the laminar flow also show that the velocity overshoot at the shear layer ($y/D = 0.5$) and above the cylinder region ($y/D > 0.5$) remains present over a longer downstream region. In the case of the turbulent incident flow, it can be seen that the velocity deficit is much smaller than that of the laminar incident flow at all the axial locations. At $x/D = 0.5$, the velocity profile results for the turbulent cases exhibit a larger velocity overshoot at the shear layer and above the cylinder region. However, moving downstream ($x/D = 1.5$), it can be noticed that the velocity overshoot for the turbulent cases decays very quickly, resulting in a more streamlined flow ($u/U_\infty \approx 1$). At farther downstream locations ($x/D = 3$ and 6), the difference between the velocity profiles of the laminar and turbulent cases becomes less significant.

The rms velocity results at $x/D = 0.5$ and 1.5 (Fig. 7e and f) show that the turbulent incident flows exhibit a higher level of velocity fluctuations than the laminar flow case, almost in the whole wake region. The results also show that the maximum velocity fluctuations occurs at the shear layer region of the cylinder ($y/D = 0.5$) for all the cases. At farther downstream location ($x/D = 6$), the velocity energy level are almost similar between the laminar and turbulent cases over a spatial

range of $0 \lesssim y/D \lesssim 2$. However, in the region above the cylinder ($y/D > 2$), *i.e.* outside the cylinder wake, it can be observed that the velocity fluctuations for the turbulent cases are still larger than that of the laminar incident flow, due to turbulence level of the incoming flow. A comparison of the results obtained using grids 1 and 2 (*i.e.* changes in the flow length scale at a fixed turbulence intensity) shows that an increase in the length scale of the flow structures does not change the velocity energy level between the grids at $x/D = 0.5$ and 1.5, *i.e.* $(u_{rms}/U_\infty)_{grid2} \approx (u_{rms}/U_\infty)_{grid1}$. In the case of grids 2 and 3 (*i.e.* changes in the turbulence intensity for a fixed length scale), results show that an increase in the level of turbulence intensity results in an increase in the level of velocity fluctuations at farther downstream location ($x/D = 6$), *i.e.* $(u_{rms}/U_\infty)_{grid3} > (u_{rms}/U_\infty)_{grid2}$.

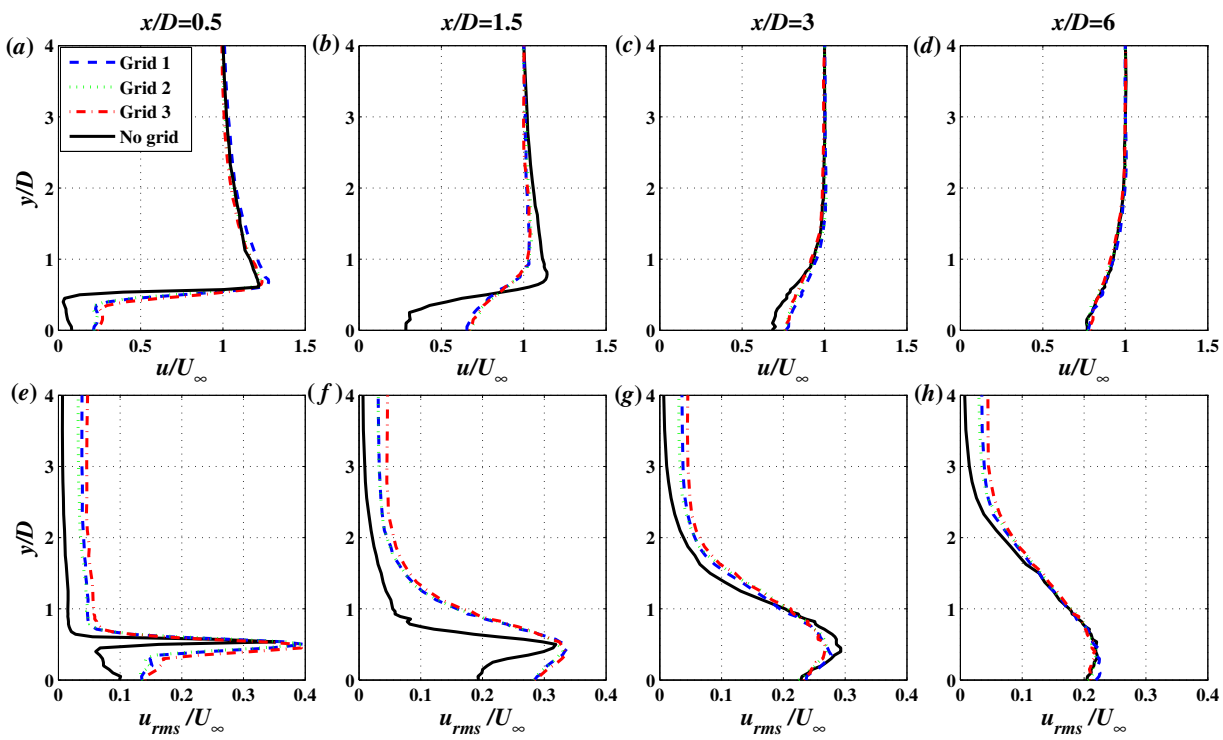

FIG. 7: Mean (a-d) and rms (e-h) velocity components in the wake of the circular cylinder.

C. Velocity power spectral density

To better understand the properties of the turbulent structures within the wake region, the energy-frequency content of the flow velocity (ϕ_{uu}) has been studied. Figure 8 shows the power spectral density (PSD) of the wake velocity as a function of the Strouhal number ($St = fD/U_\infty$) at several locations downstream of the cylinder ($x/D = 0.5, 1.5, 3$ and 6), along the centerline of the cylinder ($y/D = 0$) and several locations above the centerline of the cylinder ($y/D = 0.15, 0.57, 1.875$ and 4). The PSD calculations are performed using the Pwelch function. In order to obtain smoother and accurate results, Hamming windowing with 50% overlap is applied in the data post-processing. The frequency resolution was set to 6.4 Hz.

In the near wake region ($x/D = 0.5$ and 1.5), the fundamental vortex shedding f_0 and the first harmonic f_1 tones can be clearly seen at the wake centerline ($y/D = 0$) for the laminar flow case. Although the fundamental tone was observed at the centerline wake, the tone disappears between the centerline and the shear layer region, but eventually appears, even more clearly, at the shear layer region ($y/D = 0.57$). It can also be observed clearly that the fundamental tone protrude well above the broadband content of the spectra, particularly outside of the shear layer region ($y/D \geq 0.57$). In the case of the turbulent incident flows, the velocity PSD results show that the turbulent flows cause an increase in the energy content over the whole Strouhal range in the near wake region, which is also in agreement with the rms velocity results presented in Fig. 7. Results have also shown that the fundamental tone (f_0) can be clearly seen in the entire wake region, except at $y/D = 4$ compared to that of the laminar incident flow. The fundamental tone seems to be propagating more in the laminar flow, while in the case of the turbulent flows, the tone is dissipated more quickly over space (*i.e.* no peak is observed at $y/D = 4$). The results also show that in the near wake region, the velocity PSD spectra follow a gradient of about f^{-2} within $0.4 \lesssim St \lesssim 1$ and $f^{-3.5}$ within $3 \lesssim St \lesssim 10$ for the case with laminar incident flow, while in the case of the turbulent flows, the broadband slope changes greatly with frequency and follow a gradient of about $f^{-1.5}$ at the mid-frequencies range and f^{-3} at high frequencies. It can also be observed that the velocity PSD spectra gradient of both the turbulent and laminar incident flows are similar along the wake region, *i.e.* at the centerline, shear layer and free-stream regions.

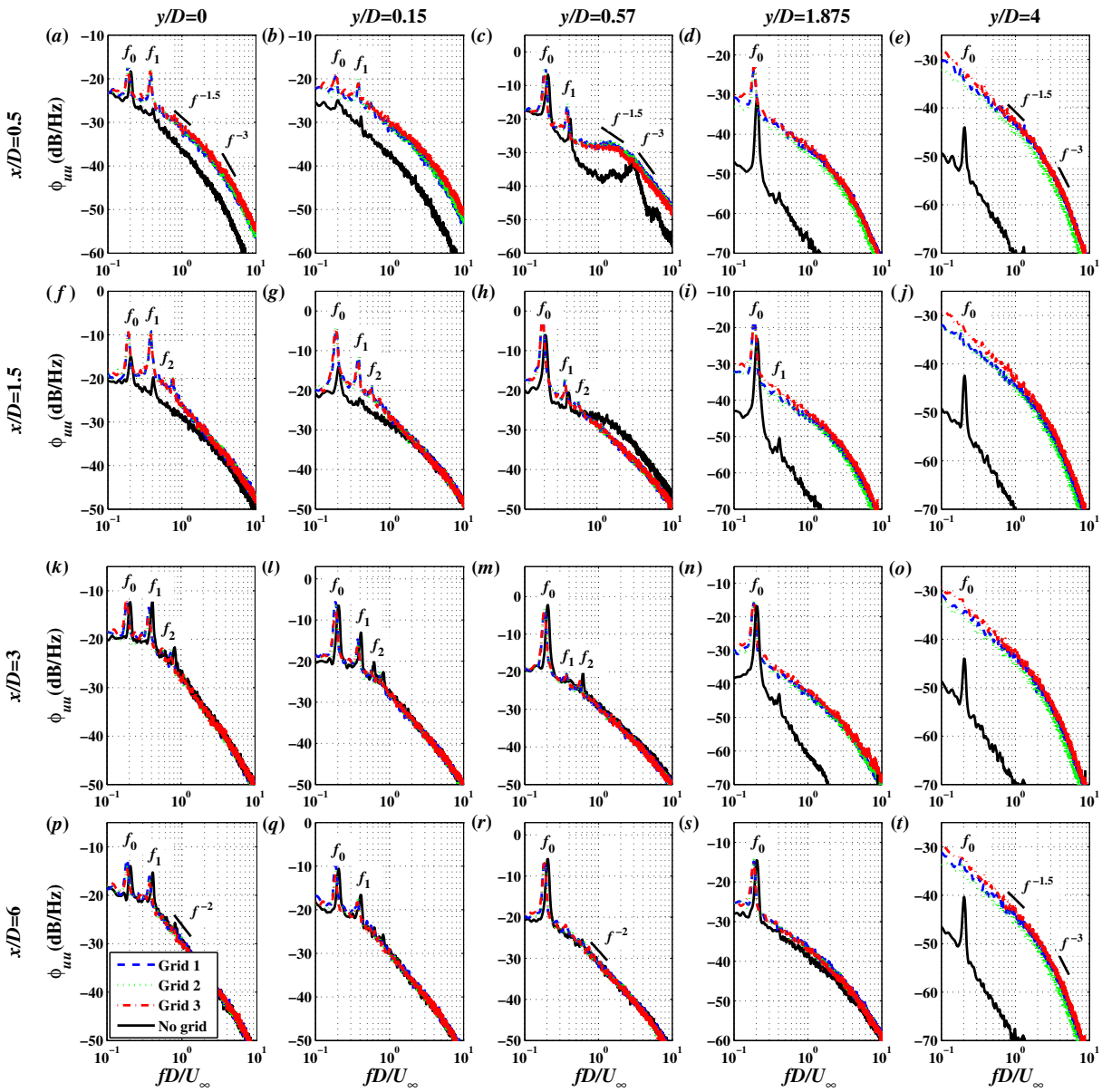

FIG. 8: Velocity power spectral density measured at different x/D and y/D locations at $Re = 14.7 \times 10^3$, *i.e.* x/D=0.5 (a-e), x/D=1.5 (f-j), x/D=3 (k-o) and x/D=6 (p-t).

In the far wake region ($x/D \geq 3$), the emergence of the fundamental, first and second harmonics of the vortex shedding frequency can be clearly seen within the shear layer region for both the laminar and turbulent flow cases. The amplitude of the fundamental vortex shedding frequency f_0 is found to be greater than that of f_1 and f_2, suggesting that f_0 has the highest energy level. It can be seen that the discrepancy between the two flows is much less between the centerline and shear layer region ($y/D = 0 - 0.15$), except at $y/D = 4$, *i.e.* outside the cylinder wake, where

the difference between the two type of flows become quite significant. Moreover, the the velocity PSD spectra at $y/D = 4$ is almost similar at all the downstream locations (*i.e.* completely outside of the shear layer), indicating that the flow in the free-stream region is turbulent, resulting in a higher broadband content, typical of turbulent incident flows. In the case of the laminar flow, the fundamental tone (f_0) is always observed at $y/D = 4$ within the wake region ($x/D = 0.5 - 6$). In the far wake region ($x/D \geq 3$), the behaviour of the spectra becomes very similar apart from a change in the magnitude of the velocity fluctuation and that the velocity PSD spectra follow a gradient of about f^{-2} for both the laminar and turbulent cases, except in the regions outside the cylinder wake.

D. Pressure power spectral density

The surface pressure power spectral density (PSD) was measured at several peripheral angles (θ), at $Re = 14.7 \times 10^3$ for the laminar and turbulent incident flow (grids 1, 2 and 3) cases. The surface pressure PSD results are presented in Fig. 9 as a function of the Strouhal number. The pressure PSD data are referenced to P_o=20 μPa. The surface pressure PSD results are presented only when the pressure fluctuations are at least 10 dB higher than the background noise due to the wind tunnel operation.

The results show that the surface pressure PSD spectra consist of both strong tonal and broadband components for both the laminar and turbulent incident flow cases. In addition to the fundamental vortex shedding frequency (f_0), the first two harmonics ($f_1 = 2f_0$ and $f_2 = 3f_0$) are also visible in the PSD results, thanks to the good signal to the background noise ratio. It can be observed from Fig. 9 that the properties of the incoming flow can cause significant changes to the vortex shedding peaks, as well as the broadband content of the exerted unsteady pressure over the cylinder. In the case of the turbulent incident flow, The results show that the fundamental tonal frequency has slightly shifted to the lower frequencies compared to the laminar incident flow. This trend is also seen at the first and second harmonics, which is consistent with the results of Hutcheson and Brooks[30]. It should be noted that the odd-numbered tones (f_0, $3f_0$, ...) are associated with the lift fluctuations of the cylinder, while the even-numbered tones ($2f_0$, $4f_0$, ...) are related to the drag fluctuations[20]. It is important to note that the oscillation frequency of a cylinder in the streamwise direction, due to the unsteady drag force is twice the vertical oscillation frequency

due to the unsteady lift force[20]. However, the amplitude of the fluctuating forces in the vertical direction are often larger than that of the streamwise fluctuating forces[20], which will be further discussed in Sec IV E and IV F. It can also be observed that the broadband energy content of the exerted unsteady pressure in the turbulent incident flow cases is generally higher than that of the laminar incident flow over the whole frequency range of interest, particularly at high frequencies and post-separation regions.

An interesting observation in Fig. 9 is that at ($\theta = 0^o$), the surface pressure PSD spectra in both the laminar and turbulent incident flow cases are completely broadband and there is no trace of any tonal component. Results show that the tonal and broadband energy content of the pressure PSD spectra increase with the angle in the pre-separation region. At $\theta = 15^o$, in the case of the laminar incident flow, the tonal component of the PSD spectra protrudes about 15 dB above the broadband content of the surface pressure, while in the case of the turbulent incident flows, the tonal components protrude about 5 dB above the broadband content of the surface pressure. In the post-separation region, it can be seen that the broadband energy content of the pressure spectra generally increases with the angle, while the tonal component of the PSD spectra protrudes even further above the broadband content of the surface pressure. It can also be observed that at the cylinder base, *i.e.* $\theta = 180^o$, the fundamental frequency at $St = 0.2$ (*i.e.* lift fluctuations) disappears, and only the first harmonic at $St = 0.4$ (*i.e.* drag fluctuations), remains as the only prominent tonal peak for both the laminar and turbulent incident flows. The amplitude of the tonal frequency at the second harmonic becomes significant only at the angles close and after the separation point ($\theta_s = 80^o, \theta_s^G = 90^o$), except at the cylinder base.

The results in Fig. 9 have also shown that the slope of the surface pressure PSD spectra changes significantly with frequency and angle ($\theta = 0^o$). However, it is not easy to find a slope for the broadband content of the surface pressure energy field at small angles and low frequencies as the PSD spectra are dominated by the tonal peaks. One can see from the results at large angles, particularly beyond the separation point, that the broadband content of the surface pressure PSD begins to increase and follow certain f^{-n} decay gradients. At low angular positions ($\theta = 0^o - 45^o$), the surface pressure PSD spectra follow a gradient of about f^{-1} and $f^{-0.5}$ within $0.1 < St < 0.4$ for the laminar and turbulent incident flows, respectively. The two types of incoming flows (laminar and turbulent), however, exhibit a similar gradient profile of about $f^{-3.5}$ and f^{-5} in the mid- and high-frequency regions, respectively, after the first harmonic. At large angles ($\theta > 135^o$), and

particularly at the cylinder base ($\theta = 180^o$), the broadband slope in the case of the turbulent incident flows changes greatly with frequency and follows a gradient of about $f^{-1.5}$ within $0.8 < fD/U_\infty < 2$ and f^{-2} at higher frequencies ($fD/U_\infty > 3$).

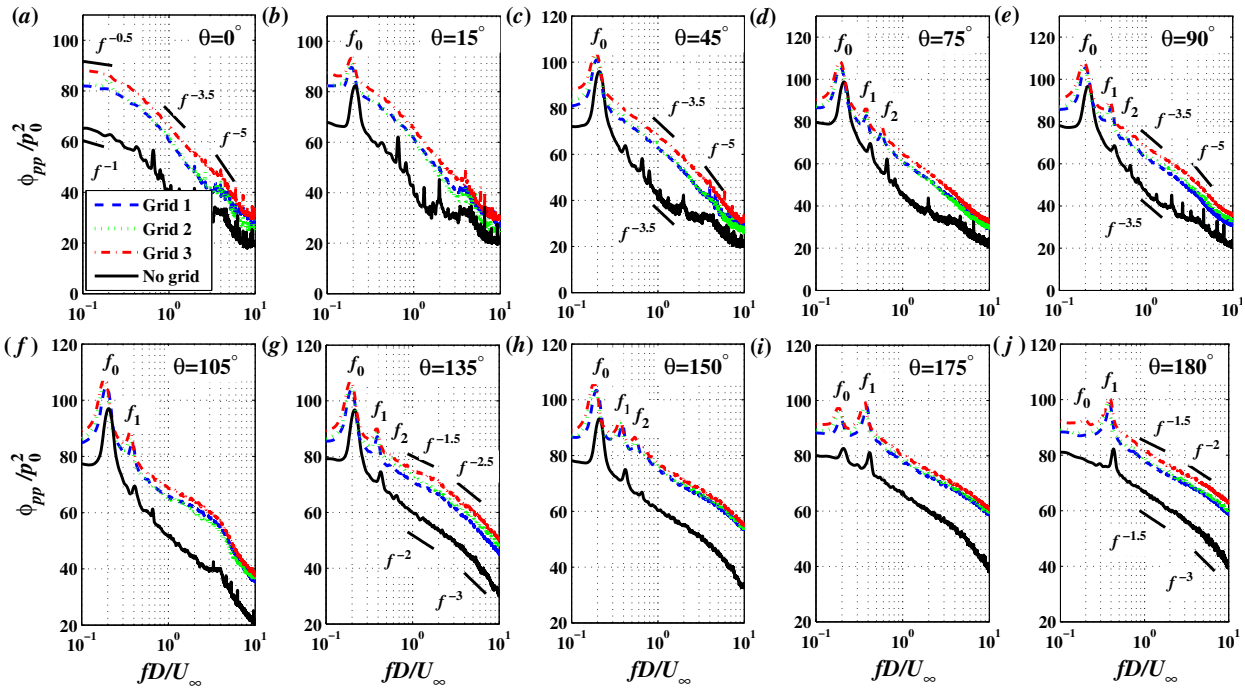

FIG. 9: Surface pressure power spectral density measured at different angular positions, $\theta = 0^o - 90^o$ (a-e) and $\theta = 105^o - 180^o$ (f-j) at $Re = 14.7 \times 10^3$.

In order to better understand the variation of the surface pressure PSD with the angle (θ), the peak amplitude of the fundamental vortex shedding frequency (f_0) and its harmonics (f_1 and f_2), obtained from Fig. 9, are extracted and presented in Fig. 10. The hollow markers denote the amplitude of the tones when they protrude above the broadband spectrum, and the filled markers show the value of the surface pressure PSD at $St = 0.2, 0.4$ and 0.6 when no clear tone is observed.

For both the laminar and turbulent incident flows, the results show that the f_0-amplitude increases with the angular position of the pressure transducers between $\theta = 0^o$ and $\theta = 75^o$. The amplitude of the fundamental peak (f_0) remains almost constant within $75^o \leq \theta \leq 135^o$ and then decreases for the angles greater than $\theta = 135^o$. The results have also shown that the difference in the amplitude of f_0 between the two flow cases remain constant at about 8 dB to 12 dB at all angular position around the cylinder. It can be observed that the amplitude of the fundamental peak (f_0),

in the case of the turbulent incident flow, experiences a sudden drop within $135^o < \theta < 180^o$, while a much more gradual decay can be seen in the case of the laminar incident flow. The fundamental tone, however, disappears completely at $\theta = 180^o$, *i.e.* extracted from the values of the broadband noise at $St = 0.2$, shown as the filled circles in the figure.

For the first harmonic ($f_1 = 2f_0$), the magnitude of the tone in the laminar incident flow increases uniformly from $\theta = 0^o$ to $\theta = 180^o$, with a small plateau region between $75^o \leq \theta \leq 135^o$. In the case of the turbulent incident flows, the f_1-amplitude is only visible for $\theta \geq 60^o$, with a plateau region within $60^o \leq \theta \leq 120^o$. A similar observation can be observed for the second harmonic ($f_2 = 3f_0$) with much lower surface pressure PSD amplitude level for all the cases (*i.e.* laminar and turbulent flows). Results have also shown that both the f_1 and f_2 tones, in laminar and turbulent incident flows, peak at around $\theta = 180^o$, while that for f_0 occurs at $\theta = 75^o$. This indicates that the fundamental vortex shedding frequency reaches the peak value near the separation point, while the first and second harmonics continue to grow into the fully separated flow and peaks at the cylinder base ($\theta = 180^o$). The results observed in Figs. 9 and 10 are particularly important for the better understanding of the noise generation mechanisms from bluff bodies in turbulent flows.

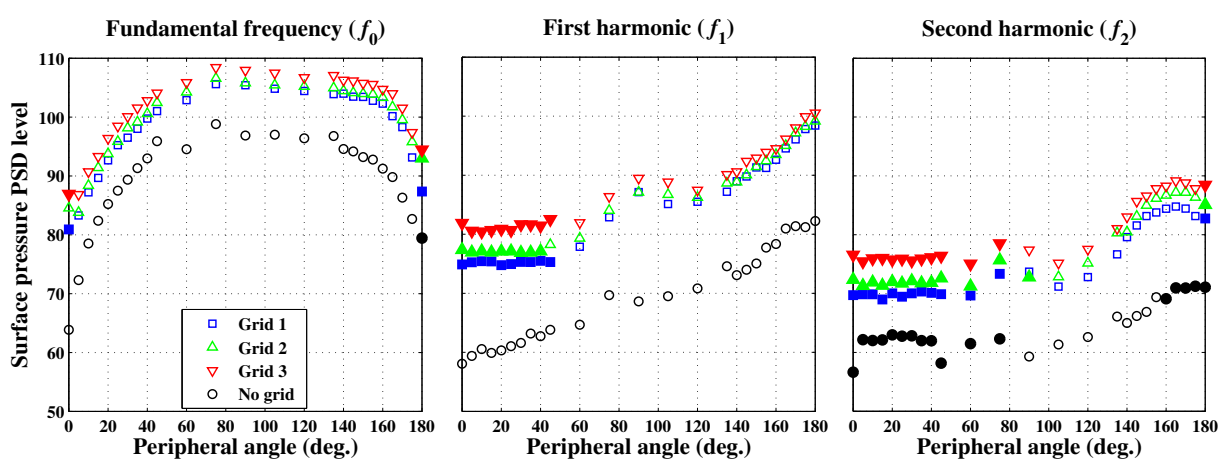

FIG. 10: Variation of the surface pressure power spectral amplitude at the fundamental vortex shedding frequency (f_0), the first harmonic (f_1=$2f_0$) and the second harmonic (f_2=$3f_0$).

A comparison of the results obtained using grids 1 and 2 (*i.e.* changes in the flow length scale at a fixed turbulence intensity) shows that an increase in the length scale of the flow structures

leads to the increase in the energy level of the tonal frequencies and the broadband content of the surface pressure PSD spectra at all angles, *i.e.* $\phi_{pp_{grid2}} > \phi_{pp_{grid1}}$. In the case of grids 2 and 3 (*i.e.* changes in the turbulence intensity for a fixed length scale), results show that an increase in the level of turbulence intensity results in the increase of the energy level of the surface pressure PSD spectra at all angles, *i.e.* $\phi_{pp_{grid3}} > \phi_{pp_{grid2}}$.

E. Lift and drag power spectral density

The lift and drag unsteady force power spectra were calculated using the unsteady surface pressure measurements, taken at every 5° over the whole circumference of the cylinder. The change in the pressure distribution can be quantified by computing the lift, $F_l(f)$ and drag, $F_d(f)$ forces from,

$$\begin{aligned} F_l(f) &= -\int p_\theta(f)\ sin\ \theta\ dA \\ &= -\frac{D}{2}\sum_i p_{\theta_i}(f)\ sin\ (\theta_i)\ d\theta, \end{aligned} \tag{4}$$

and

$$\begin{aligned} F_d(f) &= -\int p_\theta(f)\ cos\ \theta\ dA \\ &= -\frac{D}{2}\sum_i p_{\theta_i}(f)\ cos\ (\theta_i)\ d\theta. \end{aligned} \tag{5}$$

The lift and drag coefficients are then calculated using the power spectral density (PSD) of the lift and drag forces obtained from Eqs. (4) and (5), respectively. Note that, the calculation of the lift and drag PSD profile neglects the contributions of skin friction and the forces created by the loss of total pressures that may be present around the cylinder surface.

Figure 11 shows the PSD function of the lift and drag force fluctuations of the cylinder in laminar and turbulent flows. The results in Fig. 11 show that there is an overall increase in the lift and drag PSD at all frequencies in the case of the turbulent incident flows compared to that of the laminar flow, which is consistent with the overall increase observed in the $C_{p_{rms}}$ results in Fig. 6 and the surface pressure results in Fig. 9. The results in Fig. 11 have also shown that, in the case of turbulent incident flows, all the peaks observed in the lift and drag PSD results exhibit a significant broadening around the harmonic frequencies over a large frequency range compared to the laminar

flow, which is believed to be due to the three-dimensional nature of the vortex shedding process. The broadening of the vortex shedding frequency could be envisaged as the result of the turbulence in the vortex street that in some extent degrades the coherence of the vortex shedding[47,48].

The results in Fig. 11(a) show that both the fundamental vortex shedding peak (f_0) and the second harmonic peak ($3f_0$) are generated by the unsteady lift induced on the cylinder. In the case of the turbulent incident flow, despite the fact that the whole spectrum of the lift PSD experiences an increase compared to that of the laminar flow case, the amplitude of the fundamental shedding peak (f_0) relative to the broadband energy content remain fairly similar between the two flows. The second harmonic peak ($3f_0$) observed in the lift spectrum can also be seen in the velocity spectrum in the wake at the centerline and within the shear layer of the cylinder, particularly at $y/D = 0.15$ (see Fig. 8). The results have also shown that the broadband content of the power spectra of the lift fluctuations begins to increase and follows certain f^{-n} decay gradients. At the mid-frequency region, the lift PSD spectra follow a gradient of about f^{-2} within $1 < fD/U_\infty < 6$ for the laminar and turbulent incident flows, respectively. At high-frequencies, the lift PSD follows a gradient of about f^{-2} within $7 < fD/U_\infty < 12$ and f^{-4} within $10 < fD/U_\infty < 12$ for the laminar and turbulent incident flows, respectively.

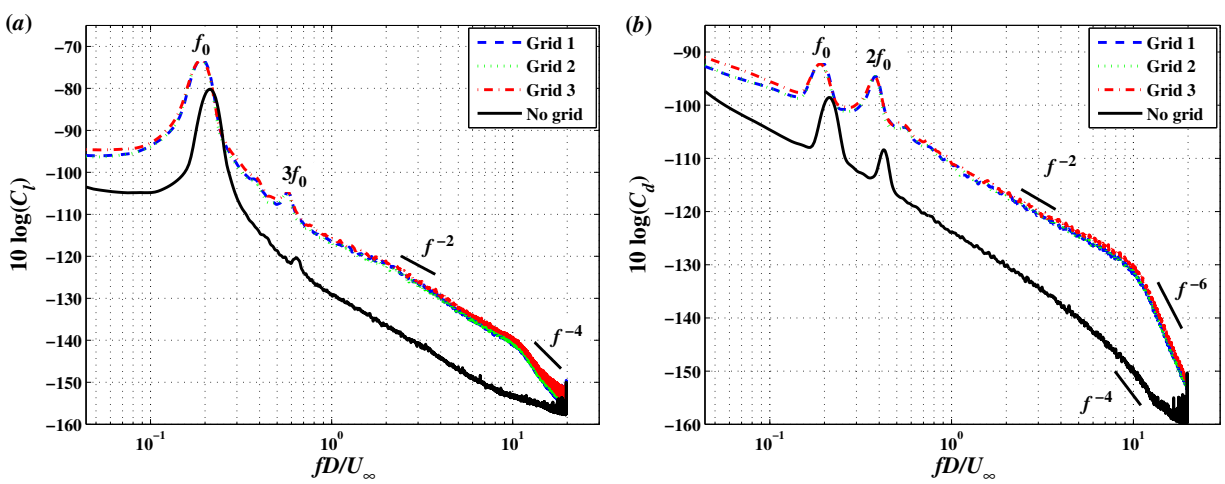

FIG. 11: (a) Lift and (b) drag power spectral density.

The results in Fig. 11(b) show that the fundamental vortex shedding peak (f_0) with a smaller magnitude can again be seen in the drag PSD results. As mentioned before, for the case of a

symmetric bluff body, the frequency of the fluctuations in the direction of the flow (*i.e.* drag) is twice the frequency of the oscillations normal to the flow direction (*i.e.* lift). The first harmonic peak ($2f_0$) observed can be related to the unsteady drag exerted on the cylinder. As seen previously in Fig. 6, the unsteady pressure acting over the base region of the cylinder cause the first harmonic ($2f_0$) observed in the drag PSD in Fig. 11. The drag PSD curves in the case of both laminar and turbulent flows, exhibit a similar profile, with a slope of about f^{-2} in the mid-frequency region after the first harmonic. The broadband slope changes greatly with frequency and follows a gradient of about f^{-4} and f^{-6} within $7 < fD/U_\infty < 12$ for the laminar and turbulent incident flows, respectively.

F. Unsteady lift and drag distribution

Figure 12 shows the distribution of the fluctuating lift and drag forces acting over the surface of the cylinder for the laminar and turbulent incident flow cases. The unsteady lift, drag and overall force are presented at the fundamental frequency (f_0) and the first three harmonics ($2f_0$, $3f_0$ and $4f_0$). In the figure, the cylinder is placed at the origin and the flow moves from the left to the right, i.e. $\theta = 0^o$ and 180° denote the stagnation and cylinder base, respectively.

Figures 12(a-d) and 12(e-f) show, respectively, the lift and drag components of the exerted unsteady pressure loading on the surface of the cylinder at the selected frequencies. As expected, the lift and drag components exhibit a dipolar pattern perpendicular to the flow direction and in the flow direction, respectively. The lift directivity pattern at f_0 is that of a proper dipole, while it gradually changes to a dipole tilted in the streamwise direction at higher frequencies. In the case of the unsteady drag force, the dipole is symmetric at f_0, but the dipole lobe on the downstream side (*i.e.* the cylinder base region) becomes larger at higher frequencies. Results have also shown that in the case of the turbulent incoming flows, the unsteady load acting on the cylinder generally increases compared to the laminar flow case, but this is more pronounced at higher frequencies. As seen in the figure, the interaction of an incoming turbulent flow with the cylinder results in roughly 8-10 dB increase in the lift and drag PSD at the dipole peak angle at the fundamental frequency (f_0) compared to the laminar flow, while that at the second and third harmonics ($3f_0$ and $4f_0$) is about 12-13 dB and 10-16 dB.

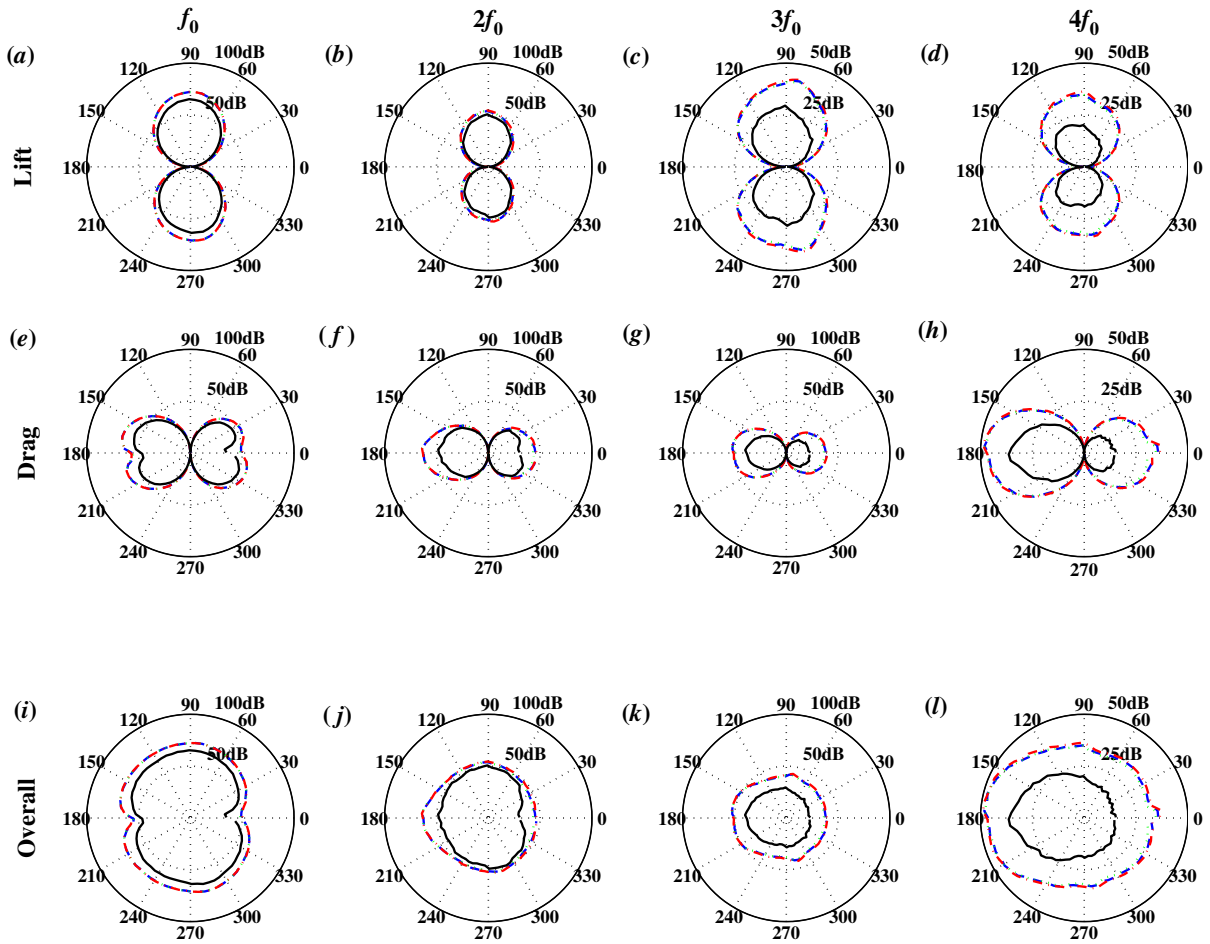

FIG. 12: Lift (a-d), drag (e-h) and overall (i-l) directivity. *Black solid line: laminar flow, blue dashed line: grid 1, green dashed line: grid 2 and red dashed line: grid 3.*

The total unsteady force acting on the cylinder as a result of interaction with laminar and turbulent flows are presented in Figs. 12(i-l). As seen, at the fundamental frequency (f_0), a symmetric distribution of the unsteady force is observed. The unsteady loading at f_0 is of a dipole shape, perpendicular to the flow direction, *i.e.* dominated by the lift fluctuations, but with no null pressure at the stagnation ($\theta = 0^o$) and the cylinder base ($\theta = 180^o$), due to unsteady drag force contribution. The incoming flow turbulence is found to increase the overall unsteady force exerted on the cylinder by about 6-7 dB at all angles. The role of the unsteady drag load and its contribution to the total unsteady force become more evident at the first harmonic ($2f_0$), particularly in the case of the incoming turbulent flows. Finally, at the second and third harmonics ($3f_0$ and $4f_0$), the loading on the cylinder takes an elliptical shape, with the base area of the cylinder experiencing the highest level of unsteady loading, mainly due to the unsteady drag component,

as seen in Fig. 11. As before, the difference of the exerted unsteady loading between the laminar and turbulent flows become more evident at higher harmonics, with 13 dB and 10 dB increase at $3f_0$ and $4f_0$, respectively.

G. Lateral coherence

In order to gain a better understanding of the tonal and broadband energy content of the coherent flow structures and the length-scale of the structures at different frequencies, the coherence between pressure signals in the spanwise direction have been studied. The coherence function between two pressure transducers along the span direction can be found from,

$$\gamma^2_{p_i,p_j}(f) = \frac{\left|\Phi_{p_i,p_j}(f)\right|^2}{\Phi_{p_i,p_i}(f)\Phi_{p_j,p_j}(f)}, \tag{6}$$

where p_i is the reference transducer and p_j is the secondary transducer at a different spanwise location, $\Phi_{p_i,p_j}(f)$ denotes the cross-spectrum between the two pressure signals, $\Phi_{p_i,p_i}(f)$ is the auto-spectrum of each individual signal. Equation 6 can be used to measure the coherence level between two pressure transducers at a fixed spanwise location, but with an angular distance of $\Delta\theta$, *i.e.* $\gamma^2(f, \Delta\theta)$.

1. Lateral coherence

The lateral coherence results measured between the spanwise transducers (p_1-p_8 in Fig. 2), with several separation distances (η) at selected angular positions (θ=0°, 45°, 90°, 135° and 180°) are presented in Fig. 13. The results are plotted as a function of the Strouhal number at a free-stream velocity of $U_\infty = 10\ m/s$ (Re=14.7×10^3) for the laminar and three turbulent incident flow cases. In order to properly capture the two- and three-dimensional flow structures around the cylinder, coherence measurements have been performed for the lateral spacings within the range of $0.41 \leq \eta/D \leq 5.95$.

As expected, the results in Fig. 13 show that the lateral coherence level between the transducers decreases with η/D at all angles. Results show that at all angles around the cylinder, the maximum coherence occurs at the fundamental vortex shedding frequency (f_0) and its harmonics (f_1 and f_2). It can also be seen that the coherence value at f_0 is greater than those at f_1 and f_2 for all angles,

except for $\theta = 180^o$, which is mainly dominated by the tonal component at f_1. The coherence values at f_0 and f_2, however, reduce to nearly zero at the base. The results have also shown that no coherence is detected for the f_1 and f_2 tones in the case of turbulent flow at the angular location of $\theta = 45^o$.

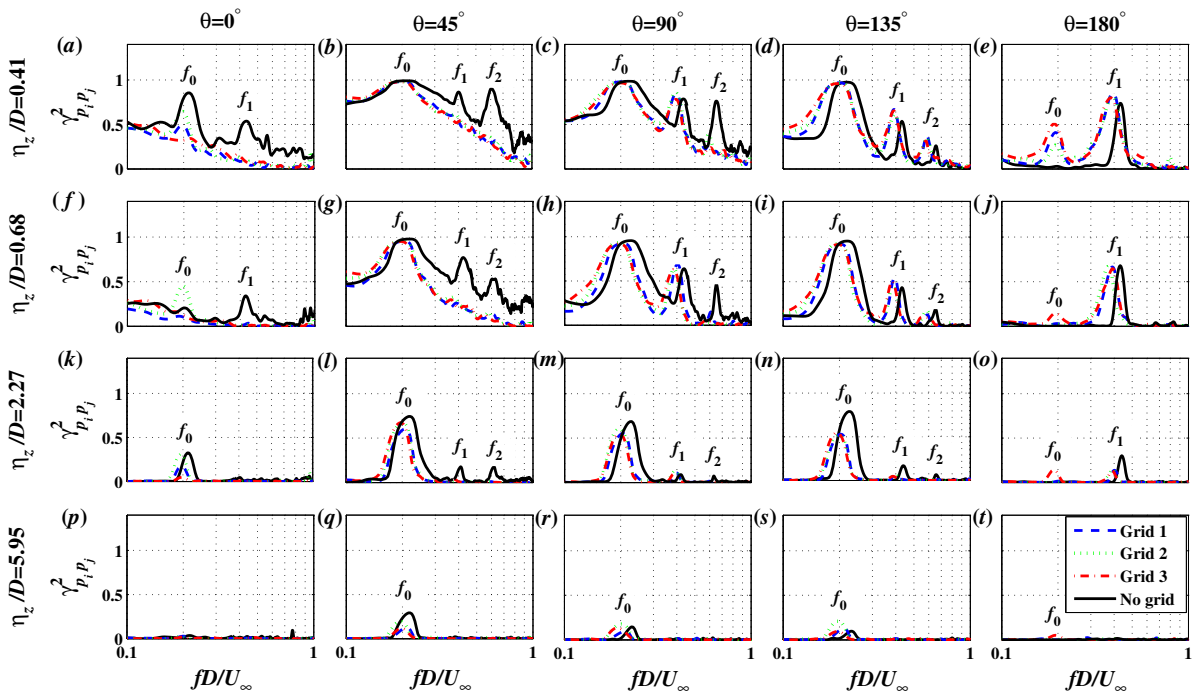

FIG. 13: Lateral coherence measured between several spanwise locations at different angular positions at $Re = 14.7 \times 10^3$, *i.e.* $\eta/D = 0.41$ (a-e), $\eta/D = 0.41$ (f-j), $\eta/D = 0.41$ (k-o) and $\eta/D = 0.41$ (p-t).

For small lateral spacings, $\eta/D = 0.41 - 0.68$, the results indicate that despite the emergence of strong peaks at f_0, f_1 and f_2, signals experience a relatively strong broadband coherence content as well. However, the coherence becomes predominantly tonal and reaches zero at other frequencies with increasing η/D, *i.e.* $\eta/D > 0.68$. This signifies that the vortex shedding structures (*i.e.* two-dimensional structures) withhold their coherence over a larger spanwise distance relative to that of the three-dimensional flow structures. The coherence of the two-dimensional structures at f_1 within $0.41 \leq \eta/D \leq 0.68$ for the turbulent incident flow is larger than that of the laminar incident flow at $\theta \geq 90^o$. This behaviour, however, can only be seen at $\theta = 90^o$ for $\eta/D \geq 0.68$.

For the lateral spacing distance of $\eta/D = 0.68 - 2.27$, at $\theta = 0^o$, the coherence results show

a broadband behaviour with a distinct tonal peak at f_0, indicating that the lift fluctuation (see Fig. 11) can be detected at the stagnation point. Moving to larger angles, the tonal and broadband contents of the lateral coherence are observed to be strongest at $\theta = 45^o$, which is believed to be due to the development of larger turbulent flow structures. The broadband coherence, however, gradually decreases at the post-separation region ($\theta = 90^o$) and within the turbulent flow region ($\theta = 135^o$) and reaches zero at $\theta = 180^o$. The results have also shown that with increasing the lateral spacing from $\eta/D = 0.68$ to 2.27, the coherence difference between the laminar and turbulent flows at f_0 increases rapidly for the angles near the separation point.

At a larger lateral spacing distance ($\eta/D = 5.95$), it can be seen that the tonal and broadband coherence for all the cases (*i.e.* laminar and turbulent incident flows) reduces to zero at $\theta = 0^o$ and $\theta = 180^o$. For the angular range of $\theta = 45^o$ to $\theta = 135^o$, a level of coherence can still be observed at the fundamental shedding frequency, indicating that vortex shedding structures retain their coherence in the post-separation and turbulent flow regions.

Figure 14 shows the lateral coherence results in terms of the transducers separation distance (η_z) at the fundamental shedding and the first and second harmonics at different angular positions for both the laminar and turbulent incident flow cases. The plot generally shows that in all cases, the coherence decays consistently with the separation distance (η_z/D). It is noticed in all cases, that the coherence is nearly one for small separation distances, indicating that the two pressure signals are perfectly correlated. in contrast, as expected , the coherence of the pressure fluctuations reduces for larger separation distances. The decay rate and the coherence level of the surface pressure fluctuations can be described using the equivalent correlation length L_c, which is defined as the spanwise distance over which the coherence drops to 0.5 [49]. The coherence data are extrapolated with a Gaussian function, *i.e.* $exp(-\alpha(\eta_z/D)^2)$, where α is the exponents constant used to determine the coherence decay rate, with the aim to calculate the correlation length L_c. The results show that the Gaussian fits the coherence data reasonably well at the fundamental vortex shedding frequency and its harmonics at all angles.

At the fundamental shedding frequency (f_0), the lateral coherence level at the stagnation point ($\theta = 0^o$) and the base of the cylinder ($\theta = 180^o$) decays much more rapidly compared to the pressure fluctuations within the laminar boundary layer and turbulence region ($\theta = 45^o, 90^o, 135^o$). At the first harmonic (f_1), the lateral coherence decay rate is much smaller than that at f_0, however, a larger coherent structures can be observed from the measurements at the base of the cylinder

($\theta = 180^o$). The results for the second harmonic (f_2) are seen to have a much higher decay rate and smaller correlation length than that of the f_0 and f_1 . The results in Fig. 14 concludes that in the case of the laminar and turbulent incident flow, the surface pressure fluctuations remains highly coherent over a long distance along the cylinder span length at the fundamental shedding frequency f_0, while for f_1 and f_2, the coherence decays much quicker over a much shorter cylinder span length. In the case of the turbulent incident flow, the coherence level at the fundamental vortex shedding frequency drops much smaller with the turbulence generated by Grid 2 and a much faster decay rate is observed with the use of Grid 3 at all angles, except at $\theta = 180^o$. The lateral coherence level at f_1 decays much faster with the use of Grid 3, while for f_2, there is no significant changes in the coherence decay rate between all the turbulence-generating grids (Grids 1, 2 and 3).

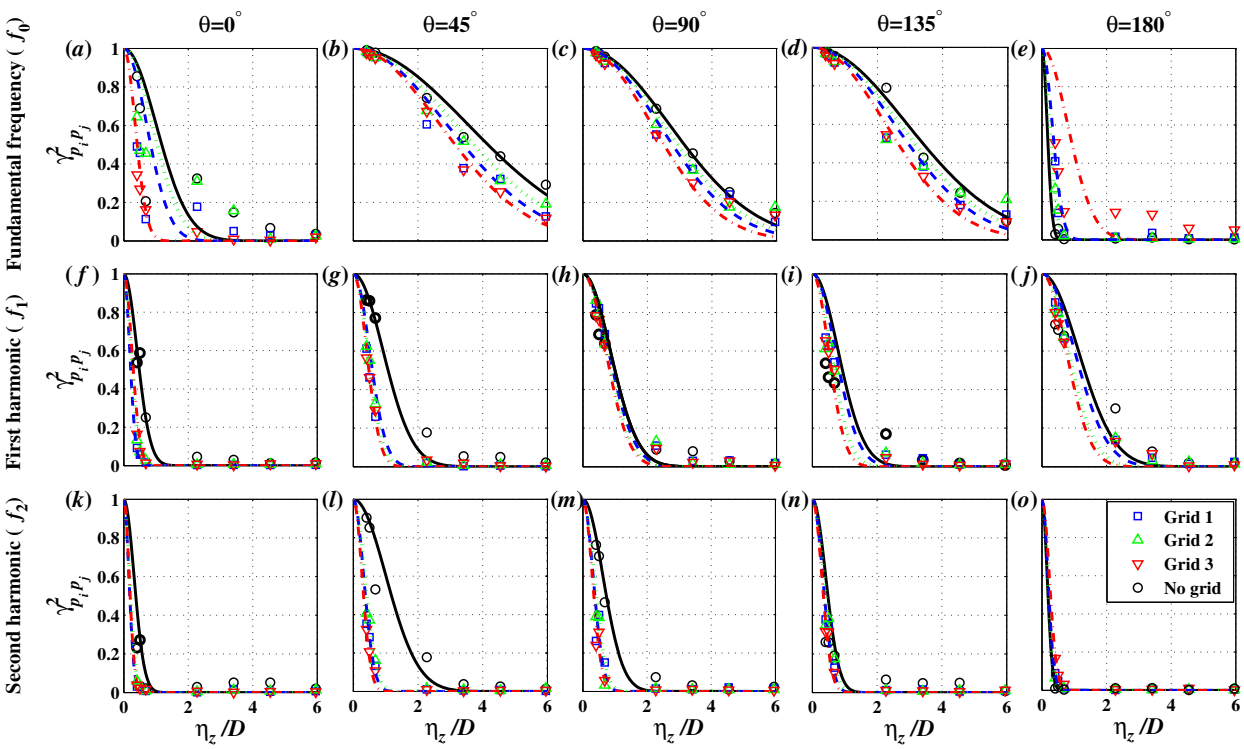

FIG. 14: Lateral coherence measured on a circular cylinder model between spanwise microphones $p1$ to $p8$ for $Re = 14.7 \times 10^3$ at the fundamental shedding (a-e), the first harmonics (f-j) and second harmonics (k-o) at different angular positions. Data are fitted with a Gaussian function ($exp(-\alpha(\eta_z/D)^2)$), shown as the solid lines.

2. *Surface pressure spanwise length-scale*

In order to understand the properties of the coherent structures passing over the cylinder in a laminar or turbulent flow, the spanwise length-scale of the flow structures as a function of frequency are studied. The spanwise length-scale of the surface pressure fluctuations along the span of the cylinder is calculated as,

$$\Lambda_{pp}(f) = \int_0^\infty \sqrt{\gamma^2_{P_i,P_j}(f,\eta)}\, dz. \tag{7}$$

Figure 15 shows the frequency-dependent spanwise length-scale results at different angles (θ). The spanwise length scale results are provided only when the pressure fluctuations are at least 10 dB higher than the background noise. In the case of the laminar incident flow, the correlation length-scale value for $\theta = 0^o$ at f_0 reaches about $\Lambda_{pp}(f_0) \approx 5D$, while that at $\theta = 45^o$, increases up to $\Lambda_{pp}(f_0) \approx 8.4D$. The correlation length-scale value at the f_1 and f_2 tones over the angular range of θ=[$45^o - 135^o$] are found to be about $\Lambda_{pp}(f_1) \approx 4.2D$ and $\Lambda_{pp}(f_2) \approx 4D$, respectively.

In the case of the turbulent incident flow, the general trend of the results at f_0, f_1 and f_2 are similar to that of the laminar incident flow, but with a smaller correlation length at all angles, except for $\theta = 180^o$, which is consistent with the coherence results observed in Fig. 13. As seen in Fig. 15(e), at the base of the cylinder ($\theta = 180^o$), no spanwise coherence is observed at f_0 in the case of the laminar flow, while in the case of the turbulent flow, the pressure signal signature of a large structure can be seen at $St = 0.2$. The results have also shown that both flow types, *i.e.* laminar and turbulent, exhibit a strong flow structure at $St = 0.4$ at the base of the cylinder ($\theta = 180^o$). The results also indicate that the two-dimensional flow structures, *i.e.* vortex shedding structures exhibit larger spanwise length-scale values relative to that of the three-dimensional flow structures, i.e. flow structures at other frequencies than that of the vortex shedding structures.

A comparison of the results obtained using grids 1 and 2 (*i.e.* changes in the flow length scale at a fixed turbulence intensity) shows that an increase in the length scale of the flow structures increases the spanwise correlation length of the flow structures at the vortex shedding frequency (f_0) at the angular location of $\theta = 0^o$. At the base of the cylinder ($\theta = 180^o$), on the other hand, the spanwise correlation length at f_0 is observed to be smaller with an increase in the length scale of the flow structures. In the case of grids 2 and 3 (*i.e.* changes in the turbulence intensity for a fixed length scale), results show that an increase in the level of turbulence intensity reduces the

spanwise correlation length at the vortex shedding frequency at the angular location of $\theta = 0^o$. However, at the base of the cylinder ($\theta = 180^o$), results show that an increase in the level of turbulence intensity leads to an increase in the spanwise correlation length at the vortex shedding frequency (f_0).

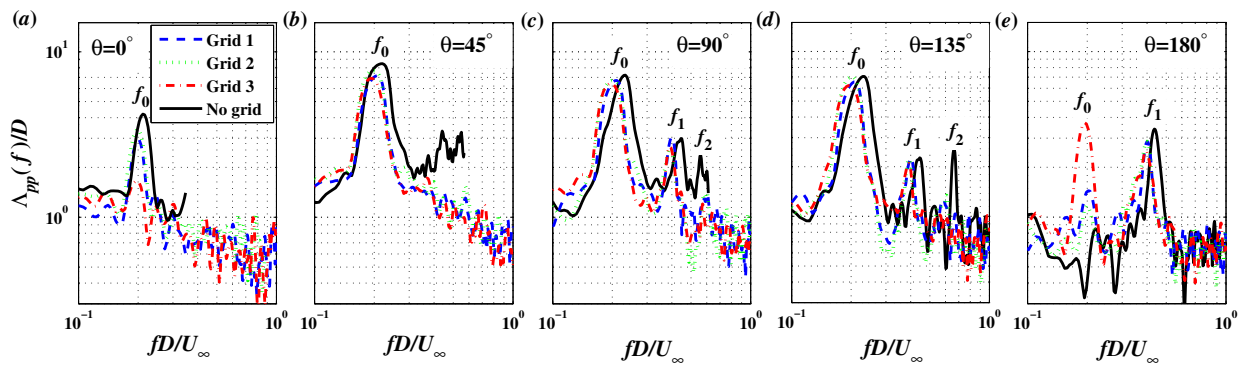

FIG. 15: Frequency-dependent spanwise length-scales of the surface pressure fluctuations at different angular position, (a) $\theta = 0^o$, (b) $\theta = 45^o$, (c) $\theta = 90^o$, (d) $\theta = 135^o$ and (e) $\theta = 180^o$ at $Re = 14.7 \times 10^3$.

V. CONCLUSIONS

A comprehensive experimental study is carried out to investigate the effects of the turbulent incoming flow on the surface pressure fluctuations acting on a cylinder in a cross-flow. The experiments have been performed using a highly instrumented setup, equipped with several peripheral and spanwise surface pressure transducers. Results show that there is a slight shift in the vortex shedding frequencies to lower frequencies in turbulent flows. The amplitudes of the fundamental tone is observed to peak within the turbulent boundary layer region and then decrease toward the base, while that of the first and second harmonics are observed to increase with the peripheral angle and peak at the cylinder base. The interaction of an incoming turbulent flow with the cylinder is shown to lead to an increase in the lift and drag PSD at the dipole peak angle at the fundamental frequency and at the second and third harmonics. The two-dimensionality of the vortex shedding structures along the cylinder span has been studied using the lateral coherence of the surface pressure fluctuations. Results show that in the case of the laminar and turbulent incident flow, the

surface pressure fluctuations remains highly coherent over a long distance along the cylinder span length at the fundamental shedding frequency f_0, while for f_1 and f_2, the coherence decays much quicker over a shorter span length.

It has also been observed that an increase in the length scale of the flow structures and the level of turbulence intensity leads to the increase in the energy level of the tonal frequencies and the broadband content of the surface pressure spectra. The spanwise coherence results have also shown that an increase in the length scale of the flow structures increases the spanwise correlation length of the flow structures at the vortex shedding frequency at the stagnation point, while at the cylinder base, the spanwise correlation length reduces at the vortex shedding frequency. The increase in the level of turbulence intensity leads to an increase in the spanwise correlation length at the vortex shedding frequency at the base of the cylinder. The results of this paper have shed light on the fundamental aerodynamics and aeroacoustics studies of bluff bodies and provide the impetus for more high-quality numerical studies.

REFERENCES

[1]R. Maryami, M. Azarpeyvand, A. Dehghan, and A. Afshari, "An experimental investigation of the surface pressure fluctuations for round cylinders," Journal of Fluids Engineering **141**, 061203 (2019).

[2]R. Maryami, S. A. Showkat Ali, M. Azarpeyvand, A. Dehghan, and A. Afshari, "Turbulent flow interaction with a circular cylinder," in *25th AIAA/CEAS Aeroacoustics Conference, AIAA 2019-2503*.

[3]S. A. Showkat Ali, M. Azarpeyvand, and C. R. I. da Silva, "Trailing-edge flow and noise control using porous treatments," Journal of Fluid Mechanics **850**, 83–119 (2018).

[4]R. Schlinker and R. AMIET, "Vortex noise from nonrotating cylinders and airfoils," in *14th Aerospace Sciences Meeting, 81* (1976).

[5]S. A. Showkat Ali, M. Azarpeyvand, M. Szőke, and C. R. Ilário da Silva, "Boundary layer flow interaction with a permeable wall," Physics of Fluids **30**, 085111 (2018).

[6]G. West and C. Apelt, "Measurements of fluctuating pressures and forces on a circular cylinder," Journal of Fluids and Structures **7**, 227–244 (1993).

[7]S. A. Showkat Ali, M. Szőke, M. Azarpeyvand, and C. R. Ilario da Silva, "Turbulent flow

interaction with porous surfaces," in *24th AIAA/CEAS Aeroacoustics Conference, AIAA 2018-2801*.

[8]E. Z. Stowell and A. F. Deming, "Vortex noise from rotating cylindrical rods," The Journal of the Acoustical Society of America **7**, 190–198 (1936).

[9]S. A. Showkat Ali, M. Azarpeyvand, and C. R. Ilario da Silva, "Trailing edge bluntness flow and noise control using porous treatments," in *22nd AIAA/CEAS Aeroacoustics Conference, AIAA 2016-2832*.

[10]S. A. Showkat Ali, M. Azarpeyvand, and C. R. Ilario da Silva, "Experimental study of porous treatment for aerodynamic and aeroacoustic purposes," in *23rd AIAA/CEAS Aeroacoustics Conference, AIAA 2017-3358*.

[11]Y. Oguma, T. Yamagata, and N. Fujisawa, "Measurement of sound source distribution around a circular cylinder in a uniform flow by combined particle image velocimetry and microphone technique," Journal of Wind Engineering and Industrial Aerodynamics **118**, 1–11 (2013).

[12]S. A. Showkat Ali, X. Liu, and M. Azarpeyvand, "Bluff body flow and noise control using porous media," in *22nd AIAA/CEAS Aeroacoustics Conference, AIAA 2016-2754*.

[13]M. Van Dyke, "An album of fluid motion," Parabolic Press Stanford (1982).

[14]L. Rayleigh, "Xlviii. aeolian tones," The London, Edinburgh, and Dublin Philosophical Magazine and Journal of Science **29**, pp. 433–444 (1915).

[15]P. Bearman and T. Morel, "Effect of free stream turbulence on the flow around bluff bodies," Progress in aerospace sciences **20**, 97–123 (1983).

[16]M. S. Bloor, "The transition to turbulence in the wake of a circular cylinder," Journal of Fluid Mechanics **19**, 290–304. (1964).

[17]C. Norberg, "Interaction between freestream turbulence and vortex shedding for a single tube in cross-flow," Journal of wind engineering and industrial aerodynamics **23**, 501–514 (1986).

[18]C. Norberg and B. Sunden, "Turbulence and reynolds number effects on the flow and fluid forces on a single cylinder in cross flow," Journal of Fluids and Structures **1(3)**, 337–357 (1987).

[19]N. Curle, "The influence of solid boundaries upon aerodynamic sound," Proceedings of the Royal Society of London. Series A. Mathematical and Physical Sciences **231**, 505–514 (1955).

[20]D. Casalino and M. Jacob, "Prediction of aerodynamic sound from circular rods via spanwise statistical modelling," Journal of Sound and Vibration **262**, 815–844 (2003).

[21]H. Fujita, H. Suzuki, A. Sagawa, and T. Takaishi, "The aeolian tone and the surface pressure

in high reynolds number flow," in *6th Aeroacoustics Conference and Exhibit, 2002* (2000).

[22]J. Ackerman, J. P. Gostelow, A. Rona, and W. E. Carscallen, "Measurements of fluctuating pressures on a circular cylinder in subsonic cross flow," AIAA Journal **47**, 2121–2131 (2009).

[23]M. M. Zdravkovich, *Flow around circular cylinders: Volume 2: Applications*, Vol. 2 (Oxford university press, 1997).

[24]A. Garcia-Sagrado and T. Hynes, "Wall pressure sources near an airfoil trailing edge under turbulent boundary layers," Journal of Fluids and Structures **30**, 3–34 (2012).

[25]J. B. Barlow, W. H. Rae Jr, and A. Pope, "Low speed wind tunnel testing," INCAS Bulletin **7**, 133 (2015).

[26]S. Yavuzkurt, "A guide to uncertainty analysis of hot-wire data," ASME, Transactions, Journal of Fluids Engineering **106**, 181–186 (1984).

[27]S. J. Wilkins and J. W. Hall, "Experimental investigation of a tandem cylinder system with a yawed upstream cylinder," Journal of Pressure Vessel Technology **136**, 011302 (2014).

[28]M. C. Goody and R. L. Simpson, "An experimental investigation of pressure fluctuations in three-dimensional turbulent boundary layers," Tech. Rep. (Virginia Tech., 1999).

[29]A. Afshari, M. Azarpeyvand, A. A. Dehghan, M. Szőke, and R. Maryami, "Trailing-edge flow manipulation using streamwise finlets," Journal of Fluid Mechanics **870**, 617–650 (2019).

[30]F. V. Hutcheson and T. F. Brooks, "Noise radiation from single and multiple rod configurations," International Journal of Aeroacoustics **11**, 291–333 (2012).

[31]J. S. Bendat and A. G. Piersol, *Random data: analysis and measurement procedures*, Vol. 729 (John Wiley & Sons, 2011).

[32]S. Corrsin, "Turbulence: experimental methods," Handbuch der Physik **3**, 524–590 (1963).

[33]P. Lavoie, L. Djenidi, and R. A. Antonia, "Effect of initial conditions on the generation of coherent structures in grid turbulence," Journal of Fluid Mechanics **346**, 201–237 (2006).

[34]E. Laws and J. Livesey, "Flow through screens," Annual review of fluid mechanics **10**, 247–266 (1978).

[35]P. Lavoie, P. Burattini, L. Djenidi, and R. A. Antonia, "Effect of initial conditions on decaying grid turbulence at low R_λ," Experiments in Fluids **39**, 865–874 (2005).

[36]P. Roach, "The generation of nearly isotropic turbulence by means of grids," International Journal of Heat and Fluid Flow **8**, 82–92 (1987).

[37]M. S. Mohamed and J. C. LaRue, "The decay power law in grid-generated turbulence," Journal

of Fluid Mechanics **219**, 195–214 (1990).

[38]G. Comte-Bellot and S. Corrsin, "The use of a contraction to improve the isotropy of grid-generated turbulence," Journal of Fluid Mechanics **25**, 657–682 (1966).

[39]S. Ling and T. Huang, "Decay of weak turbulence," The Physics of Fluids **13**, 2912–2924 (1970).

[40]R. J. Hearst and P. Lavoie, "Decay of turbulence generated by a square-fractal-element grid," Journal of Fluid Mechanics **741**, 567–584 (2014).

[41]P. Krogstad and P. Davidson, "Freely decaying, homogeneous turbulence generated by multi-scale grids," Journal of Fluid Mechanics **680**, 417–434 (2011).

[42]P. Lavoie, L. Djenidi, and R. Antonia, "Effects of initial conditions in decaying turbulence generated by passive grids," Journal of Fluid Mechanics **585**, 395–420 (2007).

[43]J. Hinze, "Turbulence McGraw-Hill," New York **218**, 457 (1975).

[44]C. Norberg, "Effects of reynolds number and a low-intensity freestream turbulence on the flow around a circular cylinder," Chalmers University, Goteborg, Sweden, Technological Publications **87**, 1–55 (1987).

[45]W. Z. Sadeh and D. B. Saharon, "Turbulence effect on crossflow around a circular cylinder at subcritical reynolds numbers," Technical Report, NASA, Washington, United States , 154 (1982).

[46]E. Achenbach, "Distribution of local pressure and skin friction around a circular cylinder in cross-flow up to $re = 5 \times 10^6$," Journal of Fluid Mechanics **34**, 625–639 (1968).

[47]I. P. Castro and L. Watson, "Vortex shedding from tapered, triangular plates: taper and aspect ratio effects," Experiments in fluids **37**, 159–167 (2004).

[48]S. R. Snarski, "Flow over yawed circular cylinders: Wall pressure spectra and flow regimes," Physics of Fluids **16**, 344–359 (2004).

[49]V. Strouhal, "Über eine besondere art der tonerregung," Annalen der Physik **241**, 216–251 (1878).

[50]M. Davis and N. Pan, "Noise generated by the interaction of turbulent jets with circular cylinders," Journal of sound and vibration **135**, 427–442 (1989).

[51]M. J. Bilka, P. Kerrian, M. H. Ross, and S. C. Morris, "Radiated sound from a circular cylinder in a turbulent shear layer," International Journal of Aeroacoustics **13**, 511–532 (2014).

[52]M. S. Uberoi and S. Wallis, "Effect of grid geometry on turbulence decay," The Physics of Fluids **10**, 1216–1224 (1967).

[53]J. Mathieu and J. Scott, *An introduction to turbulent flow* (Cambridge University Press, 2000).

[54]P. D. Weidman, *Wake transition and blockage effects on cylinder base pressures*, Ph.D. thesis,

California Institute of Technology (1968).

[55]R. Orselli, J. Meneghini, and F. Saltara, "Two and three-dimensional simulation of sound generated by flow around a circular cylinder," in *15th AIAA/CEAS Aeroacoustics Conference, AIAA 2009-3270*.

[56]A. Fage, "Further experiments on the flow around a circular cylinder," Aero. Res. Coun. **1369** (1931).

[57]E. Pang, A. Cambray, S. A. Showkat Ali, D. Rezgui, and M. Azarpeyvand, "Investigation towards a better understanding of noise generation from UAV propellers," in *24th AIAA/CEAS Aeroacoustics Conference, AIAA 2018-3450*.

[58]X. Liu, S. A. Showkat Ali, and M. Azarpeyvand, "On the application of trailing-edge serrations for noise control from tandem airfoil configurations," in *23rd AIAA/CEAS Aeroacoustics Conference, AIAA 2018-3716*.

[59]W. Elsahhar, S. A. Showkat Ali, R. Theunissen, and M. Azarpeyvand, "An experimental investigation of the effect of bluff body bluntness factor on wake-vortex noise generation," in *24th AIAA/CEAS Aeroacoustics Conference, AIAA 2018-3288*.

[60]A. Afshari, M. Azarpeyvand, A. A. Dehghan, and M. Szőke, "Effects of streamwise surface treatments on trailing edge noise reduction," in *23rd AIAA/CEAS Aeroacoustics Conference, AIAA-2017-3499*.